

# Atomic and molecular gas as traced by [C II] emission

Benedetta Casavecchia,<sup>1</sup> Umberto Maio,<sup>2,3</sup> Céline Péroux,<sup>4,5</sup> Benedetta Ciardi<sup>1</sup>

<sup>1</sup> Max-Planck-Institut für Astrophysik, Karl-Schwarzschild-Str. 1, 85748 Garching b. München, Germany

<sup>2</sup> INAF-Italian National Institute of Astrophysics, Observatory of Trieste, via G. Tiepolo 11, 34143 Trieste, Italy

<sup>3</sup> IFPU-Institute for Fundamental Physics of the Universe, via Beirut 2, 34014 Trieste, Italy

<sup>4</sup> European Southern Observatory, Karl-Schwarzschild-Str. 2, 85748 Garching b. München, Germany

<sup>5</sup> Aix Marseille Université, CNRS, Laboratoire d'Astrophysique de Marseille (LAM) UMR 7326, 13388 Marseille, France

October 21, 2024

## ABSTRACT

The latest ALMA and JWST observations provide new information on the birth and evolution of galaxies in the early Universe, at the epoch of reionization. Of particular importance are measurements at redshift  $z > 5$  of their cold-gas budget, which is known to be the main fuel for star formation. A powerful tool for probing the physics characterising galaxies at high redshift is the [C II] 158  $\mu\text{m}$  emission line. Due to its low excitation potential, [C II] emission can be produced in photodissociation regions, neutral atomic gas and molecular clouds. To properly capture the cold-gas processes taking place in such environments (molecule formation, self-shielding, dust grain catalysis, photoelectric and cosmic-ray heating), we make use of a new set of state-of-the-art hydrodynamic simulations (COLDSIM) including time-dependent non-equilibrium chemistry, star formation, stellar evolution, metal spreading and feedback mechanisms. We are able to accurately track the evolution of H I, H II and H<sub>2</sub> in a cosmological context and predict the contribution of each gas phase to [C II] luminosity. We provide formulas that can be used to estimate the mass of molecular and atomic gas from [C II] detections. Furthermore, we analyse how conversion factors evolve with galactic properties, such as stellar metallicity, star formation rate and stellar mass. We demonstrate that [C II] emission is dominated by H I gas and most of the [C II] luminosity is generated in warm, dense star-forming regions. Importantly, we conclude that, despite [C II] tracing predominantly atomic rather than molecular gas, the [C II] luminosity remains a robust indicator of the H<sub>2</sub> mass.

**Key words.** Galaxies – galaxies: evolution; Cosmology: theory – structure formation, cosmic gas

## 1. Introduction

The molecular phase, mainly composed by H<sub>2</sub>, is at the heart of the physical processes responsible in converting gas into stars as traced by the history of the star formation rate (SFR). Neutral hydrogen provides the essential fuel, but this fuel has to cool and transform to the molecular phase for star formation. These processes are often referred to as the baryon cycle (Péroux & Howk 2020).

H<sub>2</sub> detections are extremely challenging, since H<sub>2</sub> lacks of a permanent dipole moment and its lowest rotational transition requires temperatures of at least 510 K to be excited (Saslaw & Zipoy 1967; Hollenbach & McKee 1979; Lepp & Shull 1983; Galli & Palla 1998; Roussel et al. 2007; Fukui & Kawamura 2010; Dobbs & Pringle 2013; Krumholz 2014; Togi & Smith 2016). Hence, direct detections of molecular hydrogen trace a small portion of the warmer molecular gas, but not the majority of the cold one (at temperatures  $T < 10^2$  K). In this context, most estimates of molecular gas masses rely on CO rotational transitions, that enable strong and easily observable emission lines.

Through the detection of CO emission it is possible to constrain the molecular content of large samples of galaxies (Saintonge et al. 2011; Bolatto et al. 2013; Andreani et al. 2020; Tacconi et al. 2020; Boogaard et al. 2023). Unbiased surveys for molecular gas have been done with the Atacama Large Mil-

limeter/submillimeter Array (ALMA) (Decarli et al. 2019, 2020). These observations provided an assessment of the cosmic evolution of molecular gas up to redshift  $z \sim 4$  (Riechers et al. 2019; Decarli et al. 2019; Walter et al. 2022; Aravena et al. 2024). The VLA-based COLDz survey made complementary measurements at higher  $z$  (Riechers et al. 2019), while the IRAM 30 m-based xCOLD GASS provided robust  $z = 0$  measurements (Saintonge et al. 2017) and ALMACAL low-redshift measurements over a larger volume (Hamanowicz et al. 2023).

However, CO is often an unreliable tracer of H<sub>2</sub> in diffuse and low-metallicity environments (see e.g. Ebagezio et al. 2023, for recent studies). In such cases, the reduced dust content allows far-ultraviolet (UV) radiation from star-forming regions to penetrate deeply into molecular clouds and photodissociate CO molecules, creating a layer of ionised carbon (C<sup>+</sup>) around a central CO core. On the contrary, H<sub>2</sub> molecules become self-shielded from photodissociation and can survive both within C<sup>+</sup> layers and in the CO core (Krumholz & Gnedin 2011; Glover & Clark 2012; Gnedin & Draine 2014). Moreover, at higher redshift CO transitions become progressively more challenging to observe at higher frequencies (see e.g. Feruglio et al. 2023 for a broader discussion). Moreover, converting the observed CO transitions with higher rotational quantum numbers to the reference CO(1–0) introduces uncertainty, arising from variations in the poorly understood spectral line energy distribution across different galaxy types (Carilli & Walter 2013; Klitsch et al. 2019). Furthermore, the  $L_{\text{CO-to-}M_{\text{H}_2}}$  conversion factor introduces significant systematic uncertainty, and CO may no longer serve as a reliable tracer

Send offprint requests to: Benedetta Casavecchia, e-mail address: benecasa@mpa-garching.mpg.de

of  $H_2$  mass in extreme environments. Specifically, this conversion factor increases as metallicity decreases, since CO photodissociates to a larger depth in each cloud. Consequently, it varies not only between objects and with redshift (Bolatto et al. 2013), but also across different regions. Alternative indicators of molecular mass are often being used. Dunne et al. (2022) made an exhaustive comparison of the molecular-gas mass estimates from various tracers, namely: dust continuum detection, CO and CI emission lines observations. The authors conclude that the various indicators agree well within the uncertainties. The question remains whether some or all of these indicators trace the whole molecular gas, including the more diffuse component of the gas. While  $H_2$  is typically traced by CO observations, Madden et al. (2020) demonstrates that, in low-metallicity galaxies, gas is not self-shielded from UV photons and this causes the formation of a layer of [C II] emitting gas that may not be detectable through CO observations, but could still host  $H_2$ . The authors use photoionization CLOUDY modeling to emphasize that these CO-dark  $H_2$  regions can, in principle, be traced by [C II] or C I. Their findings imply that [C II] 158  $\mu\text{m}$  line emission is an excellent tracer of the total molecular gas mass in galaxies and suggest that a significant reservoir of CO-dark molecular mass might have been overlooked by previous empirical determinations. This highlights the importance of the tracer used to accurately measure molecular gas in galaxies.

The fine-structure emission line of  $C^+$  at a wavelength of 158  $\mu\text{m}$  ([C II] 158  $\mu\text{m}$ ) has proven to be a robust tracer of gas in the early Universe thanks in part to its coverage by ALMA at  $z > 4$ . Due to the low excitation potential, [C II] emission can be produced in gas with temperatures below  $\sim 10^4$  K, such as neutral atomic gas and molecular gas clouds. Three ALMA large programs in particular have observed selected UV-bright galaxies at  $z \sim 4 - 8$ . The ALPINE survey (Le Fèvre et al. 2020) has reported 118 normal star-forming galaxies at  $z = 4.5 - 6$ , and 20 of these galaxies as well as 6 more have been re-observed within the CRISTAL program (Mitsuhashi et al. 2023; Ikeda et al. 2024, Herrera-Camus et al. in prep.) in order to spatially resolve [C II] line and the far-infrared dust continuum emissions. The REBELS survey (Bouwens et al. 2022) has characterized dozens of the most luminous galaxies at  $z = 6.5 - 7.7$ . At these redshifts, direct detections of molecular gas are challenging and  $H_2$  mass ( $M_{H_2}$ ) estimates typically rely on empirical relations that link molecular gas to SFR (Kennicutt 1998; Tacconi et al. 2013), infrared luminosity (Leroy et al. 2008; Aravena et al. 2016), dust content (Rémy-Ruyer et al. 2014; Genzel et al. 2015; Tacconi et al. 2018) and dynamical mass (Daddi et al. 2010).

All these relations are well calibrated in the local Universe empirically, but are not reliable when applied at high-redshift systems. For this reason, having a physically-motivated conversion factor,  $\alpha_{[C II]}$ , that connects the [C II] luminosity ( $L_{[C II]}$ ) to the  $H_2$  mass is extremely important for an independent estimate of molecular gas mass at the epoch of reionization. Recent determinations of  $\alpha_{[C II]}$  have been provided for dwarf galaxies in the local Universe (Madden et al. 2020) and star-forming galaxies up to  $z = 2$  (Zanella et al. 2018). The  $\alpha_{[C II]}$  from Zanella et al. (2018) is frequently applied to  $z = 4 - 8$  galaxies (Béthermin et al. 2020; Schaerer et al. 2020; Tacconi et al. 2020; Dessauges-Zavadsky et al. 2020; Aravena et al. 2024), however, it is unclear if at these high redshifts [C II] detections can be solid tracers of molecular gas. Having a well calibrated method to infer  $M_{H_2}$  from  $L_{[C II]}$  is crucial for current and future observations. Indeed, this bright emission line is the target of new facilities, including the CONCERTO instrument (CONCERTO Collaboration et al. 2020; Gkogkou et al. 2023) on the Atacama Pathfinder

Experiment telescope (APEX), and future projects, such as the proposed Atacama Large Aperture Submillimeter Telescope (AtLAST) (Klaassen et al. 2020).

Additionally, the physical conditions of the gas giving rise to  $L_{[C II]}$  is still poorly understood. Establishing the dependencies on the star-forming processes and the density of the gas traced by [C II] is instrumental to a full interpretation of this emission line. Most importantly, because  $L_{[C II]}$  can be produced by ionised, atomic and molecular gas, it is challenging to interpret the wealth of new observational data without a deeper understanding of the dominant phase of the gas it traces.

On the simulations side, computing the cold phases of the gas in a cosmological context is rather demanding. On one hand, the physics involved is complex and multi-parameter; and on the other hand the resulting computing times are extremely large. This challenge is sometimes refer to as "molecular cosmology". Numerical works have investigated the physical mechanism responsible for the [C II] emission in galaxies both in the local Universe and at the epoch of reionization. Three main methods are usually adopted for modelling the [C II] luminosity. In Lagache et al. (2018) and Popping et al. (2019), the authors implemented a semi-analytical model (SAM) based on empirical relations to determine the [C II] luminosity in galaxies from the local Universe up to  $z = 7.6$  by linking their  $L_{[C II]}$  to SFR. The advantage of SAMs like those lies in the fast calculation runtime, which enables the exploration of a large parameter space. However, the simplifications inherent to SAMs can limit the accuracy of the results. An additional method relies on zoom-in simulations of single galaxies, which are typically used to resolve small-scale processes. For instance, the works by Vallini et al. (2015), Pallottini et al. (2017), Katz et al. (2019), Bisbas et al. (2022) and Schimek et al. (2024) investigate a few individual galaxies at  $z \sim 6$  with different properties, such as virial mass, metallicity, presence of mergers or not, and resolution. While zoom-in simulations provide high-resolution insights into specific galaxies, they are computationally more expensive and generally limited to a small number of cases, making it difficult to draw broad statistical conclusions. Finally, simulations run in cosmological boxes, although with lower resolution, can provide statistics on much larger samples of haloes. The works of Ramos Padilla et al. (2021, 2023) and Vizgan et al. (2022a,b) focus on modelling in post-processing the [C II] emission and the contribution coming from ionized, atomic and molecular gas phases in the EAGLE and SIMBA simulations, respectively.

Sub-grid prescriptions are crucial for modeling the cold gas phase in both zoom-in and cosmological simulations. Often, simple empirical approaches based on gas metallicity or pressure (Blitz & Rosolowsky 2006; Krumholz 2013) are used to separate neutral hydrogen into its atomic and molecular components (Lagos et al. 2015; Popping et al. 2019; Popping & Péroux 2022; Szakacs et al. 2022). Some other works employ idealized models for line emission (Olsen et al. 2018) or zoom-in simulations which, despite not including [C II] emission directly, have yielded valuable insights into the properties of individual halos (Pallottini et al. 2019). Therefore, accurately simulating the neutral and molecular phases of cold gas within a cosmological context remains one of the most critical and challenging objectives for advancing our understanding of galaxy formation and evolution at the epoch of reionization.

In this context, the COLDSIM simulation suite (see Maio et al. 2022; Maio & Viel 2023; Casavecchia et al. 2024, from now on referred to as C24) propose a novel numerical approach to investigate the physical processes underlying the  $L_{[C II]}$  emission detected in galaxies at  $z > 6$  within a cosmological frame-

work. It consists of a set of cosmological hydrodynamic simulations incorporating a time-dependent atomic and molecular non-equilibrium chemical network coupled with star formation, stellar evolution, feedback effects and cooling processes. All these features enable the capture of the mechanisms responsible for [C II] emission in galaxies. In C24 we investigated the amount of C<sup>+</sup> mass density produced in cosmic cold gas at different epochs, as well as the relations between  $L_{[\text{C II}]}$ , SFR and stellar mass.

The aim of this paper is to show that there are physically-motivated relations between  $L_{[\text{C II}]}$ , atomic hydrogen mass ( $M_{\text{HI}}$ ) and molecular hydrogen mass ( $M_{\text{H}_2}$ ). Moreover, we will investigate how conversion factors  $L_{[\text{C II}]} \text{-to-} M_{\text{H}_2}$  ( $\alpha_{[\text{C II}]}$ ) and  $L_{[\text{C II}]} \text{-to-} M_{\text{HI}}$  ( $\beta_{[\text{C II}]}$ ) evolve with galactic properties, such as stellar metallicity ( $Z_\star$ ), SFR and stellar mass ( $M_\star$ ).

The paper is organised as follows: in Section 2 we outline our methodology, while Section 3 reports our findings and relative comparisons with observational works. We discuss the impacts of our results in Section 4 and present our main conclusions in Section 5.

## 2. Method

In the following, we present the numerical simulations adopted throughout this work, how we extract the expected [C II] signal from simulated galaxies and describe how it can be related to H I and H<sub>2</sub> gas through the  $\alpha_{[\text{C II}]}$  and  $\beta_{[\text{C II}]}$  conversion factors.

### 2.1. The COLDSIM numerical simulations

For our analysis we employ the COLDSIM High Resolution (CDM HR) and COLDSIM Large Box (CDM LB) simulations described in Maio & Viel (2023) and C24, which are part of the COLDSIM suite, reported in details in Maio et al. (2022). The COLDSIM simulations have an *ad hoc* implementation to reproduce the formation of the first structures in the Universe. Differently from other approaches calibrated to reproduce local Universe properties, COLDSIM simulations are performed including chemical and physical processes typical of the early Universe. This ensures a more appropriate modeling of the pristine gas in its atomic and molecular form, and of its collapse into stars and galaxies. Gravity and smoothed-particle-hydrodynamics (SPH) computations are performed with a modified version of P-GADGET3 (Springel 2005), which includes a unique time-dependent non-equilibrium chemical network that resolves ionisation, dissociation and recombination processes of the primordial gas via first-order differential equations (Abel et al. 1997; Yoshida et al. 2003; Maio et al. 2007). In this way, we track the evolution of the following atomic and molecular species: e<sup>-</sup>, H, H<sup>+</sup>, H<sup>-</sup>, He, He<sup>+</sup>, He<sup>++</sup>, H<sub>2</sub>, H<sub>2</sub><sup>+</sup>, D, D<sup>+</sup>, HD, and HeH<sup>+</sup>. The chemical network is evolved self-consistently with stellar feedback processes, cooling and heating (Maio et al. 2022). At each time step, collisionless stellar particles are formed in a stochastic way following a modified version of the Springel & Hernquist (2003) model, in which we include molecular runaway cooling (Maio et al. 2009). Each of these particles represents a simple stellar population with a Salpeter initial mass function (IMF). We follow their stellar evolution according to mass and metallicity-dependent stellar yields and lifetimes. In particular, stellar particles produce heavy elements through Asymptotic Giant Branch (AGB) winds, Type II and Type Ia Supernova (SN) explosions (Tornatore et al. 2007; Maio et al. 2010, 2016), including He, C, N, O, Ne, Mg, Si, S, Ca, and Fe. Each of these elements is tracked individually and mixed through the SPH kernel smoothing. As detailed in Maio et al. (2022), radiative losses of metals from

resonant and fine-structure transitions, such as the [C II] emission at 158  $\mu\text{m}$ , are included in the chemical network. Primordial gas cools through H<sub>2</sub> formation via H<sup>-</sup>, H<sub>2</sub><sup>+</sup> catalysis and 3-body interactions in pristine gas, and additionally via dust catalysis in metal-enriched gas particles. The H<sub>2</sub> dust-grain catalysis is performed for different gas temperatures and metallicities, assuming a Z-dependent dust-to-metal ratio and an energy balance between the cosmic microwave background radiation and dust-grain emission with a power law of slope  $\gamma = 2$  (in agreement with recent ALMA determinations). The standard Haardt & Madau (1996) UV background generated by the formation of the first structures is turned on at  $z = 6$ . Photoelectric and cosmic-ray heating are implemented in the chemical network and complemented with H I and H<sub>2</sub> shielding (Habing 1968; Draine & Sutin 1987; Bakes & Tielens 1994; Draine & Bertoldi 1996).

Simulations are performed within the standard cosmological framework based on cold dark matter and the cosmological constant  $\Lambda$ . The present-day expansion parameter is assumed to be  $H_0 = 100h \text{ km s}^{-1} \text{ Mpc}^{-1}$  with  $h = 0.7$ , while baryon, matter and  $\Lambda$  density parameters are  $\Omega_{b,0} = 0.045$ ,  $\Omega_{m,0} = 0.274$ , and  $\Omega_{\Lambda,0} = 0.726$ , respectively. The adopted power spectrum has a spectral index of 0.96 and a normalization over an 8 Mpc  $h^{-1}$ -sphere of  $\sigma_8 = 0.8$ . In this work we adopt the notation cMpc to indicate lengths in comoving megaparsecs and, unless otherwise stated, express masses, luminosities and metallicities in solar units ( $M_\odot$ ,  $L_\odot$  and  $Z_\odot$ , respectively).

The two simulated volumes for which we report results in this paper are CDM LB and CDM HR. The former is the one with the biggest volume and is able to capture the more massive galaxies. It has a size of 50 cMpc  $h^{-1}$  and a number of particle of  $2 \times 1000^3$  evenly distributed between dark matter and gas. In CDM LB dark matter and gas particles have a mass of  $m_{\text{DM}} = 7.9 \times 10^6 M_\odot$  and  $m_{\text{gas}} = 1.6 \times 10^6 M_\odot$ , respectively. CDM HR, instead, has the highest resolution, since it has a size of 10 cMpc  $h^{-1}$  and the same number of particles, resulting in  $m_{\text{DM}} = 6.3 \times 10^4 M_\odot$  and  $m_{\text{gas}} = 1.3 \times 10^4 M_\odot$ .

### 2.2. Computing [C II] luminosities and conversion factors

In this section we describe how we estimate the [C II] emission at 158  $\mu\text{m}$  for haloes in COLDSIM. The calculations for [C II] luminosities are included directly in the simulations at runtime and contribute to cosmic-gas cooling. This guarantees that thermodynamical variables are evaluated correctly and [C II] emission is derived consistently. More detailed explanations are provided in C24, while here we limit our presentation to the most relevant methodological steps.

We consider halos composed of at least 100 particles and, for each halo,  $L_{[\text{C II}]}$  is calculated as the sum of the [C II] luminosities of each individual particle. Specifically, we model [C II] as a two-level system considering the quantum number  $J = 3/2$  and  $J = 1/2$  states for the fine-structure transition ( $2p$ ) [ $^2\text{P}_{3/2} - ^2\text{P}_{1/2}$ ]. Following Maio et al. (2007) and C24, we can write for each gas particle:

$$L_{[\text{C II}]} = \Lambda_{[\text{C II}]} V = n_{\text{C}^+,2} A_{21} \Delta E_{21} V, \quad (1)$$

where  $V$  is the volume of a sphere with radius equal to the smoothing length of the gas particle, and  $\Lambda_{[\text{C II}]}$  is the emission rate of the [C II] fine-structure transition. The quantity  $\Lambda_{[\text{C II}]}$  is expressed as a function of the number density of C<sup>+</sup> ions excited to the upper state  $n_{\text{C}^+,2}$ , the Einstein coefficient for spontaneous emission  $A_{21}$ , and the energy level separation  $\Delta E_{21}$  (for further details see e.g. Maio et al. 2007; McElroy et al. 2013, C24).



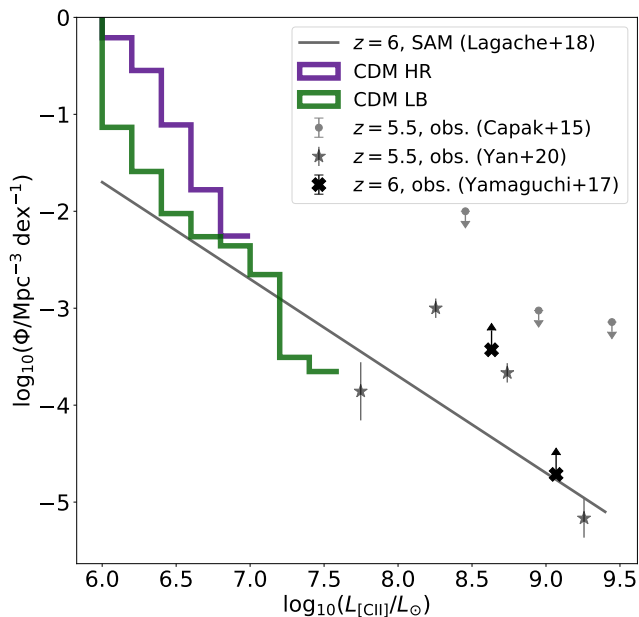


**Fig. 1.** [C II] luminosity functions at  $z = 6$ . The colored histograms represent predictions from CDM HR (purple) and CDM LB (green). The solid grey line shows the results from the G.A.S. SAM (Lagache et al. 2018). Grey symbols are ALMA data for galaxies at  $z = 5.5$  (dots, Capak et al. 2015), results from the ALPINE survey (stars, Yan et al. 2020) and lower limits from lensed [C II] line emitters at  $z = 6$  (crosses, Yamaguchi et al. 2017).

In Figure 1 we show the [C II] luminosity function  $\Phi$  for galaxies from CDM HR and CDM LB. CDM LB has lower mass resolution than CDM HR, however, thanks to its larger cosmic volume, allows us to model also more massive halos. This is clear from the higher [C II] luminosities reached in this latter case ( $\sim 10^{7.5} L_{\odot}$ ). Because of its lower resolution, CDM LB is not able to fully capture the trend of the luminosity function  $\Phi$  at the low-luminosity end, where the statistics of faint structures is underestimated by almost one dex in comparison to CDM HR. The faint end of [C II] luminosity functions seems to be sensitive to model parameters (e.g. metallicity, stellar yields, numerical resolution, star formation stochasticity, and even the way [C II] calculations are performed) as other popular diagnostics, such as UV luminosity functions (Maio & Viel 2023; Williams et al. 2024; Kravtsov & Belokurov 2024; Gelli et al. 2024). We observe, instead, a good convergence between the two simulations around  $10^7 L_{\odot}$ . We find a good agreement between the G.A.S. semi-analytical model by Lagache et al. (2018) and CDM LB, since they rely on a similar stellar-mass resolution. On the other hand, the CDM HR results are more robust in characterizing galaxies with  $L_{[\text{C II}]} < 10^7 L_{\odot}$  than G.A.S. due to the high resolution of our simulation. Thus, CDM HR is capable to capture more galaxies with fainter [C II] emission.

There are a few observational determinations at  $z = 6$  that can help constrain the [C II] luminosity function at these redshifts (Capak et al. 2015; Yamaguchi et al. 2017; Yan et al. 2020). These data were obtained with ALMA and cover luminosities slightly higher than those of COLDSIM galaxies. They have  $L_{[\text{C II}]} \gtrsim 10^{7.5} L_{\odot}$  and the resulting  $\Phi$  features a large scatter of a few dex.

In this respect, our results provide predictions for a luminosity range that is still inaccessible with current instruments. We note that Hemmati et al. (2017) have reported the first local [C II] emission line luminosity function from 500 galaxies from the Revised Bright Galaxy Sample, where the [C II] luminosities are measured from the Herschel PACS observations of Luminous Infrared Galaxies. The authors find an evolution in the [C II] luminosity function with cosmic time similar to the evolution trend of the cosmic star formation rate density.

As discussed in the Introduction,  $L_{[\text{C II}]}$  is often used as tracer of atomic and molecular gas in high  $z$  galaxies. To investigate how [C II] emission relates to different gas phases, we introduce the  $L_{[\text{C II}]}$ -to- $M_{\text{H}_2}$  conversion factor  $\alpha_{[\text{C II}]}$ , and  $L_{[\text{C II}]}$ -to- $M_{\text{HI}}$  conversion factor  $\beta_{[\text{C II}]}$ . They are defined as:  $\alpha_{[\text{C II}]} = M_{\text{H}_2}/L_{[\text{C II}]}$  and  $\beta_{[\text{C II}]} = M_{\text{HI}}/L_{[\text{C II}]}$ , where  $M_{\text{HI}}$  and  $M_{\text{H}_2}$  are the atomic and molecular hydrogen masses of each galaxy. In practice, these conversion factors are mass-to-light ratios relating [C II] to neutral gas. Usually they are reported in  $M_{\odot}/L_{\odot}$  units and allow us to link measured  $L_{[\text{C II}]}$  values to the underlying  $\text{H}_2$  or  $\text{HI}$  gas mass.

Since in this paper we aim at linking [C II] emission to atomic and molecular gas in a cosmological context, in Section 3 we will only use the highest-resolution simulation, CDM HR, if not otherwise stated.

### 3. Results

In this section we will present our results about the relations between  $L_{[\text{C II}]}$  and the different gas phases, and explore their dependence on various galactic properties, such as stellar mass, metallicity and star formation rate.

#### 3.1. Relations of $L_{[\text{C II}]}$ with atomic and molecular masses

The [C II] luminosity is often used as tracer of cold gas (with temperatures below  $10^4$  K), which is typically composed by both atomic ( $\text{HI}$ ) and molecular ( $\text{H}_2$ ) hydrogen. In this regime  $\text{HI}$  gas is expected to be dominant in mass with respect to  $\text{H}_2$ . However, due to the density and temperature dependences of the [C II] emission signal (see previous section), this does not necessarily mean that most of the  $L_{[\text{C II}]}$  is produced by neutral atomic gas.

In Figure 2 we plot  $L_{[\text{C II}]}$  as a function of  $M_{\text{H}_2}$  and  $M_{\text{HI}}$  at  $z = 10$  and 6. We observe that galaxies with higher molecular and atomic masses are more luminous in [C II]. This is expected from the cooling of atomic and molecular gas and the consequent collapse into stars, consistently with the linear trend found in C24 between the logarithms of  $L_{[\text{C II}]}$  and SFR. A similar correlation is observed in Figure 2 between  $L_{[\text{C II}]}$  vs.  $M_{\text{H}_2}$  and  $M_{\text{HI}}$  at both redshifts. The  $L_{[\text{C II}]}$  vs.  $M_{\text{H}_2}$  relation extends to higher molecular masses and  $L_{[\text{C II}]}$  at lower redshifts as a consequence of galaxy build-up through gas streams and mergers. It shows a scatter of up to  $\sim 3$  dex, suggesting that molecular hydrogen is highly sensitive to feedback processes, and thus challenging to constrain. An analogous trend is observed also for the  $L_{[\text{C II}]}$  vs.  $M_{\text{HI}}$  relation. The COLDSIM galaxies with higher  $L_{[\text{C II}]}$  are those capable of retaining more cold gas, both atomic and molecular, and fuel the global star formation activity. At all redshifts and for each  $L_{[\text{C II}]}$  values,  $M_{\text{HI}}$  is always higher than  $M_{\text{H}_2}$  by about  $\sim 2$  dex. Only a small fraction ( $\approx 10^{-2} - 10^{-1}$ ) of cold hydrogen gas becomes molecular, while the majority is atomic. Moreover, the scatter exhibited by the  $L_{[\text{C II}]}$  vs.  $M_{\text{HI}}$  relation is slightly smaller than the one from the  $L_{[\text{C II}]}$  vs.  $M_{\text{H}_2}$  relation. Below, we provide linear

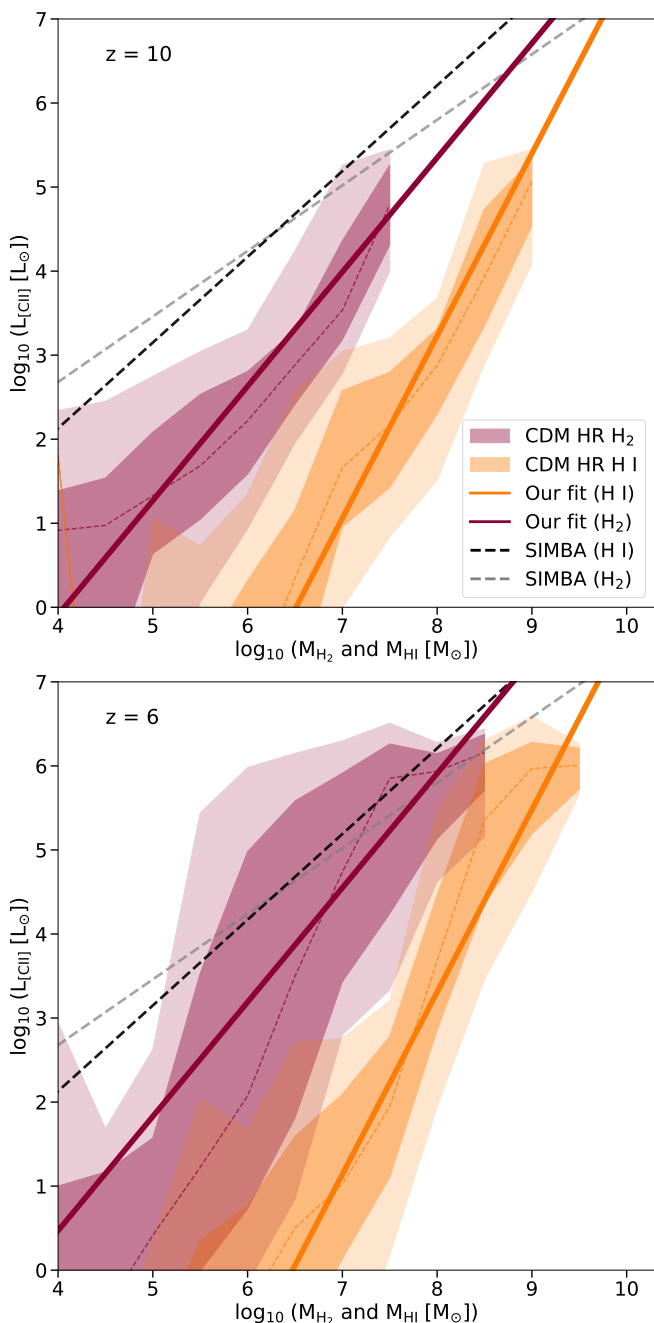


**Fig. 2.** [C II] luminosity  $L_{[\text{C II}]}$  as a function of H<sub>2</sub> mass  $M_{\text{H}_2}$  (dark pink), and H I mass  $M_{\text{H I}}$  (orange) at  $z = 10$  (top) and  $z = 6$  (bottom). The dashed lines is the mean value for CDM HR, while the darker (lighter) shaded regions represent the  $1\sigma$  ( $2\sigma$ ) standard deviation. The dark pink solid line represents the fit to the CDM HR results for  $M_{\text{H}_2}$ , while the orange solid line is the fit for  $M_{\text{H I}}$  (see the text). The dashed grey and black lines are the linear fit to post processed SIMBA simulations for  $M_{\text{H}_2}$  and  $M_{\text{H I}}$ , respectively (see Vizgan et al. 2022a,b). We highlight the redshift evolution of the linear relation between  $\log_{10}(L_{[\text{C II}]})$  and both  $\log_{10}(M_{\text{H}_2})$  and  $\log_{10}(M_{\text{H I}})$ . Moreover, we find that H I is always the dominating phase for COLDSIM galaxies.

fits, displayed in Figure 2, for the logarithms of  $L_{[\text{C II}]}$  vs.  $M_{\text{H}_2}$  and  $M_{\text{H I}}$  gas masses, that also include redshift evolution:

$$\log_{10}(L_{[\text{C II}]} / L_{\odot}) = 1.36(\pm 0.01) \log_{10}(M_{\text{H}_2} / M_{\odot}) - 0.14(\pm 0.01) z - 4.13(\pm 0.09) \quad (2)$$

$$\log_{10}(L_{[\text{C II}]} / L_{\odot}) = 1.94(\pm 0.01) \log_{10}(M_{\text{H I}} / M_{\odot}) - 0.12(\pm 0.01) z - 10.7(\pm 0.1) \quad (3)$$

Equations 2 and 3 can be used to estimate the mass of molecular and neutral hydrogen from the detected [C II] emission in high-redshift galaxies. Those expressions clearly point out that  $L_{[\text{C II}]}$  increases with H I and H<sub>2</sub> gas masses over-linearly. Furthermore, the redshift correction shows that, for any fixed mass, earlier objects have suppressed  $L_{[\text{C II}]}$  by a factor of  $\approx 10^{-0.1z}$  for both H I and H<sub>2</sub>. This is a consequence of the typically smaller metallicities encountered in primordial epochs and of their evolution towards lower  $z$ .

Our formulae can be directly compared to literature studies, such as the relations derived from the SIMBA simulations at  $z = 6$  (Vizgan et al. 2022a,b). The authors combine the output of simulations of different box sizes to cover a larger mass range, and estimate  $L_{[\text{C II}]}$ ,  $M_{\text{H}_2}$  and  $M_{\text{H I}}$  in post-processing. Their fits are computed for galaxies with molecular hydrogen mass  $M_{\text{H}_2} > 10^6 M_{\odot}$  and atomic hydrogen mass  $M_{\text{H I}} > 10^7 M_{\odot}$ . In the figure, we show their results and extrapolate them at lower H<sub>2</sub> and H I masses. COLDSIM galaxies are dominated in mass by atomic gas and the [C II] emission is mostly due to collisions with atomic hydrogen rather than molecular hydrogen. In Vizgan et al. (2022a,b), however, molecular gas is the dominant phase and the majority of [C II] emission is expected to originate by interactions with H<sub>2</sub>. The authors recognise, though, that in their model atomic gas does not contribute *by construction* to  $L_{[\text{C II}]}$ . Indeed, some of the H I gas might be hidden within the ionised gas, so the true neutral atomic mass is likely higher than indicated by their results.

In Figure 3 we show the relation between  $L_{[\text{C II}]}$  and  $M_{\text{H}_2}$  at  $z = 6$  and we compare our results with observational determinations. We report a correlation between  $L_{[\text{C II}]}$  and  $M_{\text{H}_2}$  in good agreement with a compilation of observations from the literature (Stacey et al. 1991; Díaz-Santos et al. 2013, 2017; Ferkinhoff et al. 2014; Huynh et al. 2014; Magdis et al. 2014; Capak et al. 2015; Cormier et al. 2015; Gullberg et al. 2015; Schaerer et al. 2015; Accurso et al. 2017; Contursi et al. 2017; Hughes et al. 2017; Zanella et al. 2018; Madden et al. 2020; Kaasinen et al. 2024). These observations include different types of galaxies: local dwarves, main sequence and star-forming galaxies, covering a wide range of redshift, from  $z = 0$  to 7. Although these observations cover molecular gas masses and  $L_{[\text{C II}]}$  slightly higher than those of the COLDSIM simulations, our results are consistent with data of local dwarf galaxies from Cormier et al. (2015) and Madden et al. (2020), and of main sequence galaxies from Accurso et al. (2017). The extrapolation to higher masses of our fit in equation 2 is in agreement with most observations. In addition, we compare it to the empirical fits by Zanella et al. (2018) and the fit to a model by Madden et al. (2020), which are derived from galaxies with  $L_{[\text{C II}]} > 10^7 L_{\odot}$  and  $L_{[\text{C II}]} > 10^5 L_{\odot}$ , respectively. The fit by Zanella et al. (2018) applies to lensed galaxies at  $z = 2$ , although it is routinely used to infer  $M_{\text{H}_2}$  from  $L_{[\text{C II}]}$  also for higher-redshift galaxies. This fit lays systematically above COLDSIM haloes. The one by Madden et al. (2020), instead, is derived from local dwarf galaxies, which, having metallicities and masses lower than those of more typical local galaxies, are

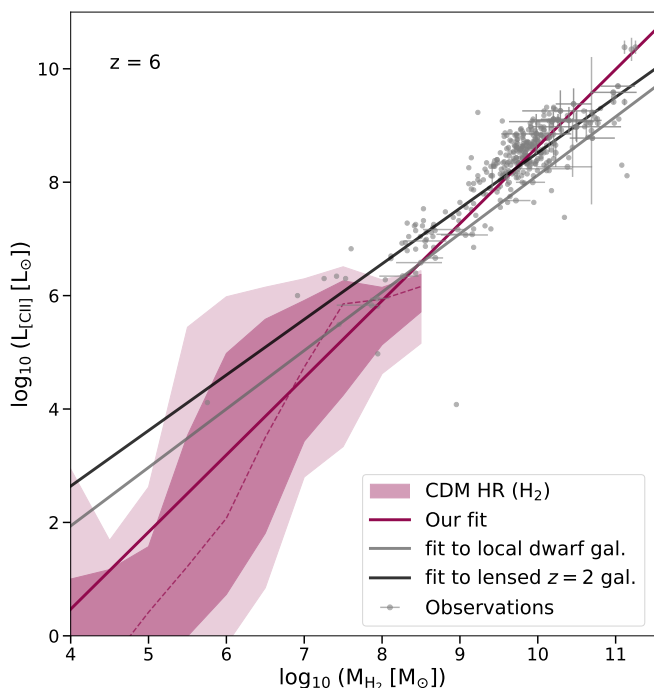


**Fig. 3.** [C II] luminosity  $L_{[\text{C II}]}$  as a function of  $\text{H}_2$  mass  $M_{\text{H}_2}$  at  $z = 6$ . The dashed line refers to the mean value for CDM HR (dark pink), while the darker (lighter) shaded region represents the  $1\sigma$  ( $2\sigma$ ) standard deviation. The dark pink solid line represents the linear fit to the CDM HR results, while the black and grey solid lines refer to the linear fits to observations from Zanella et al. (2018) and Madden et al. (2020). Grey dots represent observations of: local dwarf galaxies (Cormier et al. 2015; Madden et al. 2020),  $z = 0.5$  main sequence and starburst galaxies (Stacey et al. 1991; Díaz-Santos et al. 2013, 2017; Magdis et al. 2014; Accurso et al. 2017; Contursi et al. 2017; Hughes et al. 2017), and star-forming galaxies in the range  $z = 2 - 6$  (Ferkinhoff et al. 2014; Huynh et al. 2014; Capak et al. 2015; Gullberg et al. 2015; Schaerer et al. 2015; Zanella et al. 2018; Kaasinen et al. 2024). Globally we find that our simulations are in good agreement with observations.

usually considered as a good analogue for higher-redshift objects (Telford et al. 2023). Indeed, this fit is in better agreement with our predictions and with the conclusion that the total  $\text{H}_2$  mass is well traced by  $L_{[\text{C II}]}$ .

Finally, we highlight that our physically-motivated fits extend the empirical relations between  $L_{[\text{C II}]}$  and the mass of cold molecular gas to galaxies with [C II] luminosity  $L_{[\text{C II}]} < 10^7 L_{\odot}$ , for which observations are still missing, and provide reference for high redshift observations.

### 3.2. Conversion factors and galaxy properties

Given the linear trend of the relations presented in section 3.1, we can constrain the conversion factors  $L_{[\text{C II}]}$ -to- $M_{\text{H}_2}$ ,  $\alpha_{[\text{C II}]}$ , and  $L_{[\text{C II}]}$ -to- $M_{\text{HI}}$ ,  $\beta_{[\text{C II}]}$ . In this section we explore their dependencies on galactic properties, such as  $Z_{\star}$ ,  $M_{\star}$  and SFR. In Figure 4 we show the relation between  $\alpha_{[\text{C II}]}$  and  $\beta_{[\text{C II}]}$  and the galactic stellar metallicity  $Z_{\star}$  at  $z = 10, 8, 7$  and  $6$  combined. Both  $\alpha_{[\text{C II}]}$  and  $\beta_{[\text{C II}]}$  are roughly constant for  $Z_{\star} < 10^{-2} Z_{\odot}$ . In this regime, the scatter around both relations is large, because these low-mass haloes contain fewer gas particles.

In the range  $Z_{\star} = (10^{-2} - 10^{-1}) Z_{\odot}$  both factors experience a drop of about 2 dex in average. The reason for this is that

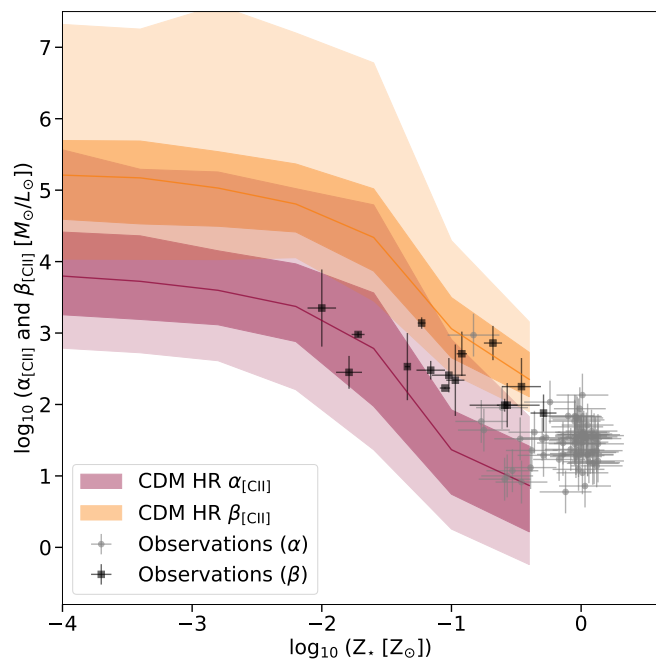


**Fig. 4.**  $L_{[\text{C II}]}$ -to- $M_{\text{H}_2}$  conversion factor  $\alpha_{[\text{C II}]}$  (dark pink) and  $L_{[\text{C II}]}$ -to- $M_{\text{HI}}$  conversion factor  $\beta_{[\text{C II}]}$  (orange) as a function of stellar metallicity  $Z_{\star}$ , at  $z = 10, 8, 7$  and  $6$  combined. The solid dark pink and orange lines represent the mean values obtained from CDM HR for  $\alpha_{[\text{C II}]}$  and  $\beta_{[\text{C II}]}$ , respectively. The darker (lighter) shaded regions represent the  $1\sigma$  ( $2\sigma$ ) standard deviation. The grey points are  $\alpha_{[\text{C II}]}$  estimates from observations of local galaxies (Cormier et al. 2015; Accurso et al. 2017; Contursi et al. 2017; Hughes et al. 2017) and  $z = 2 - 4$  galaxies (Huynh et al. 2014; Schaerer et al. 2015). Black squares are  $\beta_{[\text{C II}]}$  derived by observations of  $\gamma$ -ray burst afterglows in star-forming galaxies at  $z = 2 - 5$  (Heintz et al. 2021). COLDSIM results are in good agreement with lower redshift observations and provide predictions for future observational works. Both  $\alpha_{[\text{C II}]}$  and  $\beta_{[\text{C II}]}$  increase by  $\sim 3$  dex at low stellar metallicities.

such galaxies have experienced star formation activity (typically  $\text{SFR} > 10^{-2} M_{\odot} \text{ yr}^{-1}$ ) and stellar feedback has enriched the gas with metals, making the haloes brighter in  $L_{[\text{C II}]}$ . When an increase in [C II] luminosity is not followed by an equally efficient increase in neutral mass,  $\alpha_{[\text{C II}]}$  and  $\beta_{[\text{C II}]}$  may drop down to even lower values. At  $Z_{\star} > 10^{-1} Z_{\odot}$ ,  $\alpha_{[\text{C II}]}$  and  $\beta_{[\text{C II}]}$  are again nearly constant, with a scatter of  $\sim 2$  dex for  $\alpha_{[\text{C II}]}$  and slightly larger than 1 dex for  $\beta_{[\text{C II}]}$ . This regime represents more massive galaxies that have experienced star formation episodes and significant metal enrichment. Since they are in a more evolved stage, they have had time to restore their neutral atomic and molecular gas content, which is reflected in the shallower  $\alpha_{[\text{C II}]}$  and  $\beta_{[\text{C II}]}$  trends.

For all the metallicities, a large scatter of  $\sim 5 - 3$  dex for  $\alpha_{[\text{C II}]}$  and  $\beta_{[\text{C II}]}$  indicates that it is difficult to constrain precisely the mass of  $\text{H}_2$  and  $\text{HI}$  from  $L_{[\text{C II}]}$ , as also displayed in Figure 2. We find a good agreement between our estimates of  $\alpha_{[\text{C II}]}$  with observations of galaxies with  $Z_{\star} > 10^{-1} Z_{\odot}$  in the range  $z = 0 - 4$  (Huynh et al. 2014; Cormier et al. 2015; Schaerer et al. 2015; Accurso et al. 2017; Contursi et al. 2017; Hughes et al. 2017), especially with the local dwarf galaxies described in Cormier et al. (2015). Moreover, we compare our results of  $\beta_{[\text{C II}]}$ , with observations of star-forming galaxies at  $z = 2 - 5$  by Heintz et al. (2021), finding a good agreement for metallicities  $Z_{\star} > 10^{-1.5} Z_{\odot}$ . At lower metallicities the COLDSIM simula-

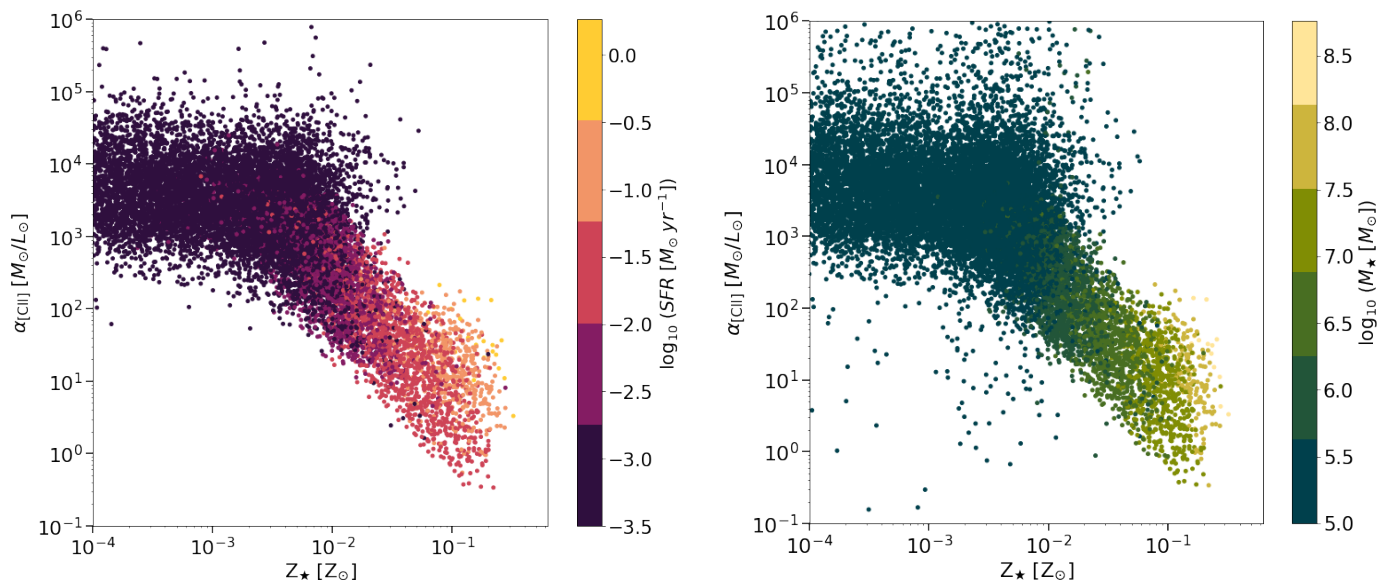


**Fig. 5.** Conversion factor  $\alpha_{[\text{C II}]}$  as a function of stellar metallicity  $Z_{\star}$  color coded according to SFR (left panel) and stellar mass (right panel) for COLD SIM galaxies. We highlight that the scatter around the relations presented in Figure 4 is mainly affected by the SFR at  $Z_{\star} > 10^{-2.2} Z_{\odot}$ .

tions predict higher values of  $\beta_{[\text{C II}]}$ . This might be due to the fact that Heintz et al. (2021) estimate  $M_{\text{HI}}$  from  $\gamma$ -ray bursts, probing mainly the very dense gas ( $N_{\text{H}} > 10^{21} \text{ cm}^{-2}$ ), while our values take into account also the diffuse H I retained in the galaxies. Early work from Vizgan et al. (2022b) reports a trend with metallicity which is consistent with the findings presented here. Our theoretical results can be useful for observational work in order to constrain the role metallicity plays in determining the trend of conversion factors. Especially, for low metallicity galaxies, our findings explore a regime in which observations struggles in characterising molecular and atomic gas masses.

To better understand the trend and scatter of  $\alpha_{[\text{C II}]}$  as a function of  $Z_{\star}$ , in Figure 5 we show the same relation, colour-coded according to SFR (left panel) and stellar mass (right panel). Galaxies with  $Z_{\star} < 10^{-2} Z_{\odot}$  have typically  $\text{SFR} < 10^{-2.2} M_{\odot} \text{ yr}^{-1}$  and  $M_{\star} < 10^6 M_{\odot}$ . These haloes are cold and poor in metals, and their  $L_{[\text{C II}]}$  is faint. For higher metallicities, however, the drop in  $\alpha_{[\text{C II}]}$  coincides with an increase in SFR and  $M_{\star}$ . Indeed, as also demonstrated in C24, more massive and star-forming galaxies are also richer in metals and thus in carbon. However, while masses vary by one or two orders of magnitude,  $L_{[\text{C II}]}$  can vary by four or five dex (see e.g. previous Figure 2).

Regarding the wide scatter of  $\sim 3$  dex at  $Z_{\star}$  above  $10^{-2} Z_{\odot}$ , we observe for a fixed metallicity a larger scatter in SFR. For example, galaxies with higher SFR exhibit values of  $\alpha_{[\text{C II}]}$  larger than those of quiescent galaxies in the same  $Z_{\star}$  bin. This is a result of the stellar feedback, so galaxies which are more star-forming are also hotter, with a mass weighted temperature above  $\sim 10^5 \text{ K}$ . Therefore, in these haloes carbon is present in higher ionisation levels and  $L_{[\text{C II}]}$  decreases. This effect implies  $\alpha_{[\text{C II}]}$  values for galaxies with  $\text{SFR} \sim 1 M_{\odot} \text{ yr}^{-1}$  to be up to 2 dex larger than those of galaxies with  $\text{SFR} \sim 10^{-1.5} M_{\odot} \text{ yr}^{-1}$  at a given  $Z_{\star}$ . We do not notice such a strong dependence of the scatter on the stellar masses at fixed metallicity, in agreement with the tighter mass-metallicity relation discussed in e.g. C24.

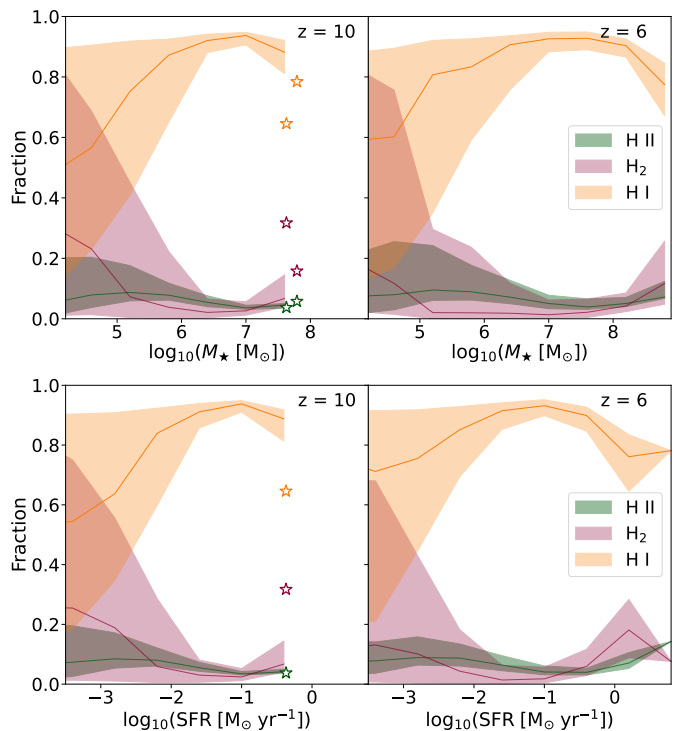


**Fig. 6.** Contribution to the [C II] luminosity from H I (orange), H<sub>2</sub> (dark pink) and H II (green) as a function of stellar mass (top row) and star formation rate (bottom row) at  $z = 10$  (left panels) and 6 (right). The solid line displays the median values, while the shaded areas the  $1\sigma$  scatter. The stars represent the contribution from the three phases in bins with fewer than three galaxies. The [C II] emission traces mostly neutral atomic gas.

### 3.3. Gas phases traced by [C II] emission

As mentioned in the previous sections,  $L_{[\text{C II}]}$  is in general a powerful tracer of cold gas. In this regime, different gas phases may coexist, though. Cold gas typically hosts both atomic (H I)



and molecular ( $\text{H}_2$ ) hydrogen, as well as residual ionised  $\text{H I}$  gas. As mentioned above, although at temperatures below few  $10^4$  K the  $\text{H I}$  mass is expected to be dominant with respect to  $\text{H}_2$  and  $\text{H II}$  masses, it is not obvious which gas phase could be associated to most of  $[\text{C II}]$  emission, due to the density and temperature dependences of  $L_{[\text{C II}]}$ .

The contribution to the  $[\text{C II}]$  luminosity from each gas phase (ionised, molecular and atomic) is shown in Figure 6 as a function of  $M_\star$  (top panel) and SFR (bottom panel). In order to compute how much each gas phase contributes to the total  $L_{[\text{C II}]}$  of a galaxy, we decompose the total  $[\text{C II}]$  emission (eq. 1) into its components (eq. 2 in C24) for each gas particle, and then sum up  $L_{[\text{C II}]}$  particle contributions in each galaxy. We specify that the contribution in luminosity arising from  $\text{H II}$  gas is mainly due to interactions with electrons.

We note that at each redshift most of the  $[\text{C II}]$  emission is generated by collisions with  $\text{H I}$ . However, the contribution of each phase varies with  $M_\star$  and SFR. At all redshifts, for stellar masses between  $10^5$  and  $10^{7.5} M_\odot$  and SFR of  $10^{-2}$  to  $10^{-0.5} M_\odot \text{ yr}^{-1}$ , the contribution to  $L_{[\text{C II}]}$  from collisions with  $\text{H I}$  is approximately 90%, with  $\text{H II}$  that can reach up to 10%, while the contribution from  $\text{H}_2$  is often negligible. In practice, stellar feedback makes these galaxies brighter in  $L_{[\text{C II}]}$ , until gas particles reach temperatures higher than a few  $10^4$  K. Hotter temperatures are reached in galaxies with  $M_\star > 10^{7.5} M_\odot$  and SFR  $> 10^{-0.5} M_\odot \text{ yr}^{-1}$  (right panels in the figure). As a result, these galaxies have  $L_{[\text{C II}]}$  that does not increase with stellar mass or SFR, and therefore present a lower  $\text{H I}$  contribution than less massive and star-forming galaxies. This decrease in  $\text{H I}$  contribution is compensated by an increase in the fraction of  $L_{[\text{C II}]}$  produced by  $\text{H}_2$  (up to almost 30%) instead of  $\text{H II}$  (a few percents). These haloes in fact have large values of  $M_{\text{H}_2}$ , as can be seen in Figure 2. By contrast, in gas particles with higher temperatures and dominated by ionised gas, carbon is excited at higher ionisation levels. Haloes with  $M_\star < 10^6 M_\odot$  and SFR  $< 10^{-2} M_\odot \text{ yr}^{-1}$  show a remarkable scatter. As already mentioned in previous sections, these small and quiescent galaxies are more susceptible to feedback effects and this makes the scatter around median values larger.

Our COLDSIM simulations suggest that  $L_{[\text{C II}]}$  largely traces atomic  $\text{H I}$  gas. This result is different from some interpretations of observations in the literature which conclude that  $\sim 60 - 80\%$  of the  $[\text{C II}]$  emission arises from  $\text{H}_2$  gas (Pineda et al. 2013; De Breuck et al. 2019). Our findings are a non-trivial consequence of the  $[\text{C II}]$  emission properties and the fact that  $\text{H I}$  is the dominant species in gas below  $\sim 10^4$  K, while  $\text{H}_2$  is predominant in rarer cold and dense regimes. This result is valid at any redshift and stellar metallicity for galaxies with  $M_\star > 10^5 M_\odot$  and SFR  $> 10^{-2.5} M_\odot \text{ yr}^{-1}$ , and it is in agreement with observational estimates (e.g. Croxall et al. 2017; Cormier et al. 2019). In particular, we find a good agreement with the recent results of Ikeda et al. (2024) from the CRISTAL survey on 34 spatially resolved galaxies in the range  $z = 4 - 6$ . The authors argue that the extended  $[\text{C II}]$  emission in half of the sample originates in the diffuse medium, either  $\text{H I}$  or  $\text{H II}$ . We also emphasise that, although  $L_{[\text{C II}]}$  largely traces the atomic  $\text{H I}$  gas phase, this is not in contradiction with our conclusions about the  $L_{[\text{C II}]}$  vs.  $M_{\text{H}_2}$  relation in Section 3.1 and previous observational claims by e.g. Madden et al. (2020) or Zanella et al. (2018). Indeed,  $L_{[\text{C II}]}$  can be a robust indicator of the mass of molecular gas, notwithstanding the typically smaller amounts of  $\text{H}_2$  in this temperature regime. In fact,  $[\text{C II}]$  correlates with cooling and clumping of gas, which in turn enhance  $\text{H}_2$ -driven star formation, increases collisional excitation and, consequently, emissivity.

### 3.4. $[\text{C II}]$ relation to dense and star-forming gas

In this section we discuss the contribution of star-forming gas to the  $[\text{C II}]$  emission and characterize how different regimes in terms of density and temperature contribute to the total  $L_{[\text{C II}]}$  in the simulated box. This is often done for the sake of simplicity by various works which do not explicitly distinguish the gas into its molecular or atomic form, but into star-forming/not-star-forming and dense/diffuse gas.

In table 1 we display in the first row the fraction of  $L_{[\text{C II}]}$  originated in star-forming parcels which have SFR  $> 0 M_\odot \text{ yr}^{-1}$  ( $f_{[\text{C II}], \text{SF}}$ ) at  $z = 10, 8, 7$  and 6. Moreover, we divide gas particles in three different phases: diffuse (diff, with  $n_{\text{H}} < 10 \text{ cm}^{-3}$ ), cold dense (CD, with  $n_{\text{H}} > 10 \text{ cm}^{-3}$  and  $T < 10^4$  K), and warm dense (WD, with  $n_{\text{H}} > 10 \text{ cm}^{-3}$  and  $10^4 \text{ K} < T < 4 \times 10^4$  K). We choose  $4 \times 10^4$  K as upper limit for the WD phase since particles hotter than that do not emit in  $[\text{C II}]$  (see C24 for more details). From such definitions, we then compute the fraction of  $L_{[\text{C II}]}$  coming from the different regimes (i.e.  $f_{[\text{C II}], \text{SF}}$ ,  $f_{[\text{C II}], \text{diff}}$ ,  $f_{[\text{C II}], \text{CD}}$  and  $f_{[\text{C II}], \text{WD}}$ , respectively). We find that, at each redshift, most of the  $[\text{C II}]$  emission is generated by star-forming and WD gas, as displayed in table 1. This result is not surprising because star-forming particles have usually number densities above  $10 \text{ cm}^{-3}$  and are also close to WD particles, since stellar feedback quickly brings temperatures above  $10^4$  K. This result indicates how stellar feedback is essential to produce  $[\text{C II}]$  emission in our simulations. On one side, gas is enriched with metals, including carbon, by SN explosions and AGB winds. On the other side, this gas has the physical conditions in terms of density and temperature to excite  $[\text{C II}]$  for the emission at  $158 \mu\text{m}$ . The increase in contribution from WD and star-forming gas from  $z = 10$  to  $z = 6$  is in line with the increasing SFR density reported in C24, showing that there is more and more gas in the simulation turning into stars. Moreover, in C24 we found that  $[\text{C II}]$  can be used to trace star formation in the same redshift range.

This result might be sensitive to star formation and feedback prescriptions, metal enrichment details, as well as particle resolution. Different-resolution runs, in fact, resolve differently gas regions that are dense enough to emit radiation via  $[\text{C II}]$   $158 \mu\text{m}$  fine-structure line. In Schimek et al. (2024), for example, the authors study the fraction of  $L_{[\text{C II}]}$  emitted by dense particles with  $n_{\text{H}} > 10 \text{ cm}^{-3}$  and  $T < 10^4$  K, and by diffuse gas particles at lower densities. They examine a zoom-in simulation of a single galaxy at redshift  $z = 6.5$  and compute the  $[\text{C II}]$  luminosity in post-processing, finding that most of the  $L_{[\text{C II}]}$  originates from dense particles, although a large percentage of 44% is emitted by more diffuse gas. Recent results by Gurman et al. (2024) show that most of the  $[\text{C II}]$  emission is produced by warm medium, that they define as gas with  $n_{\text{H}} > 10 \text{ cm}^{-3}$  and temperature of  $3 \times 10^3 \text{ K} < T < 3 \times 10^4 \text{ K}$ . They perform high-resolution hydrodynamical simulations of a patch of the interstellar medium (pixel resolution of about 2 pc) including  $\text{H}_2$  chemistry and Type II SN feedback, and post-process their simulated gas cells to infer carbon abundances and  $L_{[\text{C II}]}$  signal. They find that the most of the  $[\text{C II}]$  luminosity is originated by warm neutral medium and  $\text{H II}$  regions. This result is not affected by metallicity, however it may vary with the choice of the temperature upper limit and with more detailed treatments of low-temperature metal cooling and feedback.

## 4. Discussion

The conversion of molecular gas into stars is traced by the depletion time, which is based on the ratio between  $\text{H}_2$  gas mass



**Table 1.** Fraction of [C II] luminosity produced in gas particles with  $\text{SFR} > 0 M_{\odot} \text{yr}^{-1}$  ( $f_{[\text{C II}], \text{SF}}$ ), in diffuse gas with  $n_{\text{H}} < 10 \text{ cm}^{-3}$  ( $f_{[\text{C II}], \text{diff}}$ ), in cold dense gas with  $n_{\text{H}} > 10 \text{ cm}^{-3}$  and  $T < 10^4 \text{ K}$  ( $f_{[\text{C II}], \text{CD}}$ ), and in warm dense gas with  $n_{\text{H}} > 10 \text{ cm}^{-3}$  and  $10^4 \text{ K} < T < 4 \times 10^4 \text{ K}$  ( $f_{[\text{C II}], \text{WD}}$ ) at  $z = 10, 8, 7$  and  $6$ .

	$z = 10$	$z = 8$	$z = 7$	$z = 6$
$f_{[\text{C II}], \text{SF}}$	0.72	0.92	0.96	0.97
$f_{[\text{C II}], \text{diff}}$	0.36	0.04	0.04	0.04
$f_{[\text{C II}], \text{CD}}$	0.12	0.04	0.04	0.02
$f_{[\text{C II}], \text{WD}}$	0.52	0.92	0.92	0.94

and SFR. From a theoretical perspective it is difficult to properly model the physical processes involving molecular gas. In fact, various scales need to be considered, ranging from large-scale cosmological environments to interstellar physics on parsec scale. In this context, our work is intended to both understand the origin of the measured  $L_{[\text{C II}]}$  signals and support observers especially in interpreting the properties of galaxies detected with facilities such as ALMA and JWST.

In the following, we first discuss assumptions and caveats of our COLDSIM numerical simulations, then compare our results with other numerical works in the literature and, finally, we show how our work can be useful for observational studies in accurately estimating molecular gas mass in high- $z$  galaxies.

#### 4.1. COLDSIM assumptions and caveats

Our simulations, like all others in the literature, rely on a number of assumptions that affect the quantitative results shown in this paper. We stress that the adoption of a detailed non-equilibrium model for chemical abundance calculations, similar to the one used here, is crucial to capture the processes shaping atomic and molecular gas, as highlighted by e.g. Davé et al. (2020) or Hu et al. (2021).

Possible caveats caused by the choices in the set-up have been extensively described in e.g. Maio et al. (2022), Maio & Viel (2023) and C24. There, we have already discussed the main assumptions about the initial stellar metallicity, different models of explosive nucleosynthesis and stellar-wind variations of the values of carbon yields by up to 1 dex, as well as the atomic-physics uncertainties in the collisional rates needed to calculate [C II] luminosity.

Sources of uncertainty may arise from the way stellar feedback is implemented. In COLDSIM each stellar particle is considered as a stellar population with a Salpeter (Salpeter 1955) initial mass function. Other IMF models, such as Chabrier (Chabrier 2003), which are more bottom heavy, would inject more  $\alpha$  elements from Supernova Type II explosions into the surrounding medium. This can be seen, for example, by considering the Supernova Type II fraction of the two IMFs, which is  $\sim 0.2\%$  for a Salpeter and  $\sim 3\%$  for a Chabrier. As far as our study is concerned, the choice of the IMF might have an impact on  $L_{[\text{C II}]}$ , since the mass of ejected carbon depends on the slope of the IMF. In contrast, we do not expect the choice of a Chabrier over a Salpeter IMF to have strong consequences on the values of  $M_{\text{HI}}$  and  $M_{\text{H}_2}$ . In fact, Maio et al. (2022) analysed both IMFs and did not notice any significant differences in the primordial H<sub>2</sub> and H I cosmological mass density.

In addition, our stellar feedback model assumes that also population III (Pop III) stars are distributed with a Salpeter IMF, similarly to population II (Pop II) and I (Pop I) stars. However, dif-

ferent choices for the early Pop III IMF are possible. For example, in case of a top-heavy Pop III IMF, primordial stars would have a much shorter lifetime than Pop II and Pop I stars. Consequently, at high redshifts they would enrich the interstellar medium with metals more quickly (see results in e.g. Maio et al. 2010), with possible implications for early [C II] luminosities.

Besides Type II SNe, in this work we also consider AGB stars and Type Ia SNe, that are driven by lower-mass stars with longer lifetimes. Their typical timescales are of the order of  $10^8 - 10^9$  yr, thus they can enrich the cosmic medium already by  $z \approx 6$ . This has direct implications for feedback effects and chemical abundances during the epoch of reionization (as demonstrated by the first spectroscopic evidence of a mature stellar population in a  $z \approx 8$  galaxy, A2744-YD4; Witten et al. 2024). As an example, AGB stars produce relevant amounts of carbon in only few hundreds Myrs, therefore both gas chemical patterns and the expected [C II] emission may be severely affected by them. The metal yields of Type Ia SNe do not strongly depend on the initial stellar metallicity, nonetheless their occurrence requires timescales that go from less than  $10^8$  to more than  $10^9$  yr and assumptions about the realization probability of the Type Ia SN scenario. This latter is basically unknown for early epochs, thus, we have relied on standard prescriptions suggested by stellar-evolution models (for usual stellar parameters the delay time distribution peaks well below one Gyr; Tinsley 1980; Greggio 2005; Maoz & Graur 2017). In this way we are able to take into account their possible impact on our [C II] luminosity estimates, as well. We stress that these concerns about AGB enrichment and Type Ia SNe must be kept in mind when focusing on primordial metal signatures, since most high-redshift numerical simulations tend to neglect them (although roughly half Type Ia SNe in a single stellar population explode within less than a Gyr; Cappellaro et al. 2015).

In our work, galactic winds take place at a fixed velocity of 350 km/s and are temporarily decoupled from cooling and star formation (according to Maio et al. 2011a). This allows us to obtain more efficient mass ejection, mitigate potential overcooling problems and, at the same time, prevent unphysical behaviours related to the formation of stars in the wind phase. Uncertainties about wind velocities (or mass loading factors) are large, however we have checked that at these early epochs the exact adopted value has no drastic effects for H I and H<sub>2</sub> phases, due to the relatively small mass of the hosting haloes (Maio et al. 2022). At intermediate and low redshifts the impacts might be more relevant, though Nagamine et al. (2004), while a decrease in outflow velocity might lead to more prominent galactic blue peaks at  $z > 6$  (Hassan & Gronke 2021).

Throughout this paper, we do not consider feedback from primordial black holes (BHs). Their presence would possibly cause displacement in the gas, creating turbulence and heating the surrounding medium. Besides the huge uncertainties in early-BH models, it is possible that this effect could reduce the amount of cold gas, particularly in its molecular form, causing the baryons to be in a hotter phase. However, at these redshifts the masses of BHs are expected to be smaller than those in the local Universe and, if the BH mass-bulge mass relation still holds, their masses should be at most  $\sim 10^{-3}$  times the hosting stellar masses (see detailed figures in C24). Severe implications from early BH seeds would be found only in very extreme cases, such as the ones discussed in e.g. Woods et al. (2024), Patrick et al. (2023) and Maio et al. (2019). Thus, we believe that, in general, including primordial BHs should not have drastic consequences for our findings.

In COLDSIM heavy elements produced by stars are spread over the neighbouring particles, and metal mixing is mimicked

through SPH kernel smoothing. This means that, in a low-density region at higher distances from the point of origin of the metals, the metallicity might be underestimated. This is typical of many SPH simulations, though, and winds are usually helpful to alleviate this problem. Since we focus on cold-gas phases and particles close to star-forming regions, this effect should not have significant consequences on our results.

Variations in the adopted cosmological parameters, higher-order corrections to linear theory, or in the assumed dark-matter scenario are likely to play a minor role, since [C II] emission comes essentially from cold gas that is bound within the structure potential wells and does not feel long-distance cosmological effects. They might alter high-redshift statistics, though (for a deeper discussion on the topic see e.g. Yoshida et al. 2003; Maio et al. 2006, 2011b; Maio & Viel 2015, 2023, and references therein).

#### 4.2. Comparison with other numerical studies

Numerically, one of the greatest challenges is to accurately model physical processes responsible for the [C II] fine-structure line emission at  $158 \mu\text{m}$  in a cosmological context. COLDSIM has a non-equilibrium chemical network implemented on the fly and designed to describe primordial gas chemistry. Specifically, at each time step the abundances of each atomic and molecular gas species are computed in a consistent way with cooling and heating processes. Moreover, individual elements, including carbon, are tracked separately and not inferred from a global metallicity. This means that the amount of carbon in each particle is estimated at each simulation time-step according to the underlying stellar-evolution model. This state-of-the-art set-up enables the calculation of the contribution of each gas phase, ionised, atomic and molecular, to the [C II] emission.

As the results discussed in this paper are sensitive to the implementation adopted to track the different gas phases, here we compare our findings with those from other numerical work in the literature. We emphasise that the various models differ in terms of initial set-up, box size, resolution, feedback implementation, sub-grid physics and post-processing of  $L_{[\text{C II}]}$  and gas phase contributions.

Previous works have investigated the contribution of different gas phases to the [C II] emission in galaxies at high  $z$  via semi-analytical models (Vallini et al. 2015; Lagache et al. 2018; Popping et al. 2019; Yang et al. 2022), zoom-in simulations of individual galaxies (Olsen et al. 2017, 2018; Pallottini et al. 2019; Lupi & Bovino 2020; Bisbas et al. 2022; Schimek et al. 2024) or a section of interstellar medium (Gurman et al. 2024), and post-processing of cosmological simulations (Ramos Padilla et al. 2021, 2023; Vizgan et al. 2022a,b; Garcia et al. 2023). All these investigations are naturally based on a number of different assumptions and sub-grid models that can lead to large discrepancies in the results. For example, with the exception of Olsen et al. (2017, 2018), Lupi & Bovino (2020), and Bisbas et al. (2022), all the others trace a global metallicity and infer the carbon mass in post-processing. COLDSIM instead follows individual elements according to stellar evolution and the associated gas cooling self-consistently. Additionally, as it is computationally expensive to include  $\text{H}_2$  processes in the chemical network as here, only few works did it and for single halos, either implementing [C II] emission as well (Bisbas et al. 2022) or neglecting it (Pallottini et al. 2017, 2019).

There are only a handful of studies that investigate the contribution of different gas phases to  $L_{[\text{C II}]}$  at the epoch of reionization through cosmological simulations. All these works estimate the

$\text{H I}$  and  $\text{H}_2$  masses in post-processing, though. Here, we mention Vizgan et al. (2022a,b); Garcia et al. (2023) with SIMBA, and Ramos Padilla et al. (2021, 2023) with EAGLE. They cover box sizes ranging from  $25 \text{ cMpc}/h$  to  $100 \text{ cMpc}/h$ .

As described in Section 3.1, our results robustly indicate that there is a linear correlation between the logarithms of  $L_{[\text{C II}]}$  and those of  $M_{\text{H}_2}$  and  $M_{\text{HI}}$ . Previously, this relation had only been studied via [C II] post-processing modeling by Vizgan et al. (2022a,b). The slope and amplitude of their relations are different from ours, but the range of masses and luminosities from which our and SIMBA's fits are derived are different.

Another important result concerns how the different galaxy properties, including  $L_{[\text{C II}]}$ , molecular and atomic gas mass, SFR, metallicity and stellar mass, evolve with redshift. In this respect, Liang et al. (2024) studied the empirical  $L_{[\text{C II}]}$ -SFR relation with the FIRE cosmological zoom-in simulations, focusing especially on the so called "[C II] deficit galaxies". The authors report two distinct physical regimes:  $\text{H}_2$ -rich galaxies, where the depletion time is the main driver of the [C II] deficit; and  $\text{H}_2$ -poor galaxies, where gas metallicity dominates. Consistently with C24, their findings suggest that the [C II] deficit is a widespread characteristic of galaxies, highlighting the need for caution when using a constant  $L_{[\text{C II}]}$ -to-SFR conversion factor — derived from local star-forming galaxies — to estimate SFRs at high redshifts (see, e.g., Righi et al. 2008; Sommovigo et al. 2021; Roy & Lapi 2024).

In our study, we investigate how the conversion factors  $\alpha_{[\text{C II}]}$  and  $\beta_{[\text{C II}]}$  depend on galactic properties. We find that both conversion factors are dependent on stellar metallicity,  $Z_\star$ . Additionally, for  $Z_\star > 10^{-2} Z_\odot$ , galaxies with larger  $\alpha_{[\text{C II}]}$  are those with higher SFR, outlining how the conversion factor depends strongly on the galaxy's star formation activity.

In Section 3.3 we show that  $\text{H I}$  is the gas phase that dominates [C II] emission, while the  $\text{H}_2$  gas phase can contribute for no more than  $\sim 30\%$  to a galaxy  $L_{[\text{C II}]}$ . Thus, some of the previous findings (such as the ones by Vallini et al. 2015; Lupi & Bovino 2020; Ramos Padilla et al. 2021, 2023; Bisbas et al. 2022; Gurman et al. 2024) are in agreement with ours.

For the sake of simplicity, a number of works do not explicitly distinguish the gas into molecular or atomic, but into star-forming/not-star-forming and dense/diffuse (Schimek et al. 2024; Gurman et al. 2024). Lately, Di Cesare et al. (2024) have speculated that in galaxy mergers at  $z > 4$  about 50% of the [C II] emission might come from the diffuse medium originated in the middle of the merger and suggest that even at lower redshifts [C II] emission from diffuse gas is not negligible. In Muñoz-Elgueta et al. (2024), the authors study the [C II] emission in a sample of 357 galaxies between redshift 4 and 6. They show that the majority of  $L_{[\text{C II}]}$  is originating from the dense star formation sites, while the [C II] extended emission comes from satellite galaxies or outflows within the virial radius. We note once again that different simulations and post-processing methods provide non-converging results.

In addition to these numerical efforts attempting to characterise  $M_{\text{H}_2}$  with  $L_{[\text{C II}]}$ , others are using CO emission. Among them, Hu et al. (2023) presented high-resolution ( $\sim 0.2 \text{ pc}$ ) hydrodynamical simulations of an isolated low-metallicity ( $0.1 Z_\odot$ ) dwarf galaxy coupled with a time-dependent chemistry network. This metallicity regime is of particular relevance to the high-redshift objects which are now unrevealed by JWST (Curtis-Lake et al. 2023). On a cosmological scale, Keating et al. (2020) used the FIRE zoom-in simulations to reproduce the  $L_{\text{CO}}$ -to- $M_{\text{H}_2}$  conversion factor. They relied on an equilibrium solver for estimating  $\text{H}_2$  and CO abundances on post-processing and reported little evolution of the  $L_{\text{CO}}$ -to- $M_{\text{H}_2}$  conversion factor with SFR,

contrary to our non-equilibrium findings about the  $L_{[\text{C II}]}$ -to- $M_{\text{H}_2}$  conversion factor.

#### 4.3. Predictions for high- $z$ observations

Observationally, there are many works that find a linear relation between  $L_{[\text{C II}]}$  and the mass of H<sub>2</sub> in the local Universe and then estimate a conversion factor. Nevertheless, it is complicated to estimate it empirically at high redshift or at low metallicities. In fact, in these regimes it becomes challenging to observe metal emission lines or to infer the mass of molecular gas without relying on  $L_{[\text{C II}]}$ . The maximum redshift reached to estimate  $\alpha_{[\text{C II}]}$  from galactic gas is  $z \approx 4$  (Huynh et al. 2014), however, the hosting objects are usually very luminous ( $L_{[\text{C II}]} > 10^9 L_{\odot}$ ), massive in H<sub>2</sub> and are not statistically representative of the majority of high-redshift galaxies, which are less luminous and have smaller masses. For galaxies at the epoch of reionization, when CO cannot be observed, a conversion factor of  $\alpha_{[\text{C II}]} = 31 M_{\odot}/L_{\odot}$  empirically derived by Zanella et al. (2018) from star-forming lensed galaxies at  $z = 2$  is often applied. Indeed, Dessauges-Zavadsky et al. (2020); Aravena et al. (2024) and Kaasinen et al. (2024) use this value to estimate the H<sub>2</sub> mass of galaxies in the redshift range  $z = 4 - 8$ . In Kaasinen et al. (2024), the authors also show how estimates of  $M_{\text{H}_2}$  can vary by more than one dex depending on whether [C II] or CO emissions are used as tracers. Moreover, Glazer et al. (2024) find that low-mass galaxies at  $z \approx 7$  present a deficit in [C II] luminosity when their  $L_{[\text{C II}]}$  is compared to the expectations by the  $L_{[\text{C II}]}$ -SFR relation calibrated on local dwarf galaxies (e.g. De Looze et al. 2014). The authors justify this conclusion by invoking the low metallicities of their sample compared to those of the local Universe. This result therefore indicates that galaxies at high  $z$  might have different properties from those at lower redshift and would require a physically-motivated  $\alpha_{[\text{C II}]}$  calibration.

Our findings highlight that  $L_{[\text{C II}]}$  is dominated by the H I atomic phase of the gas in high-redshift galaxies. Nonetheless, it is important to note that this result does not imply that all available H I interacts with carbon and produces  $L_{[\text{C II}]}$ . Obviously, the H I gas should be more extended than the [C II] region, which requires ionising photons with energy greater than 11.3 eV, as also observed in nearby galaxies (Péroux et al. 2019; Szakacs et al. 2021). Moreover, pristine gas, such as the one that is far from star-forming regions, could be rich in H I, but contain no metals (hence would not emit any  $L_{[\text{C II}]}$  signal). This is particularly true in primordial galaxies, when the amount of pristine material is expected to be greater than in the local Universe, and that is why we need a  $L_{[\text{C II}]}$ -to- $M_{\text{HI}}$  conversion factor  $\beta_{[\text{C II}]}$  computed at  $z > 6$  that evolves with metallicity.

Our work is useful for estimating the mass of cold gas, atomic and molecular, in galaxies at the epoch of reionization, such as those of the ALPINE and REBELS surveys. Furthermore, it would be interesting to understand how [C II] emission is spatially distributed with respect to H I and H<sub>2</sub>. This type of analysis will be very useful in view of the new results from, e.g. the CRISTAL survey. In fact, the CRISTAL project targets 34 galaxies in the range  $z = 4 - 6$  and spatially resolves their [C II] emission. So far, our simulations are in agreement with recent results by Ikeda et al. (2024), who find extended [C II] emission primarily linked to star formation activity, with contributions from atomic gas and mergers that can further expand the [C II] line distribution.

Finally, in order to check the observability of the simulated objects, we compute the exposure time needed for detecting COLDSIM galaxies with the ALMA 12 m array. For this purpose we use the CASA sensitivity calculator (McMullin et al.

2007) and check the time required to detect at  $5\sigma$  the most luminous galaxies in our sample. We select [C II] emission at  $z = 6$ , corresponding to an observed frequency of 271.5 GHz, observable in ALMA Band 7. To detect a galaxy with  $L_{[\text{C II}]} \sim 10^7 L_{\odot}$ , the exposure time needed results in seven hours on source, or less for lower redshifts. Our predictions indicate that, although it is still challenging to probe such galaxies, with physical properties predicted by COLDSIM, more massive haloes would be within reach of ALMA.

## 5. Conclusions

It is not yet possible to observationally resolve the spatial distribution of cold gas and estimate the masses of H I and H<sub>2</sub> components in galaxies at the epoch of reionization. An important tool for tracing atomic and molecular gas at these redshifts is the fine-structure 158  $\mu\text{m}$  [C II] emission line observed by state-of-the-art facilities such as ALMA and within the reach of the future AtLAST project. However, at these epochs it is still unclear which phase of the gas is mostly responsible for [C II] luminosity, whether ionised, neutral atomic or molecular, and what the high- $z$  trends of the corresponding mass-to-light ratios are.

In this work, we have extended our previous numerical analysis (Casavecchia et al. 2024) and explored the processes responsible for [C II] emission by using selected runs from the COLDSIM numerical simulations (Maio et al. 2022; Maio & Viel 2023; Casavecchia et al. 2024). These are cosmological simulations that include, in addition to the usual implementation of gravity and hydrodynamic calculations, a physics-rich and accurate non-equilibrium chemical network that follows the evolution of atomic and molecular species, in particular the ones which we focus on here: H I, H II and H<sub>2</sub>. Primordial chemistry is computed consistently with star formation and feedback effects, as well as cooling and heating processes. With COLDSIM we can track the time evolution of individual heavy elements, including carbon, and consequently derive [C II] emission from collision processes with H I, H II and H<sub>2</sub>. In this way, we are able to provide physically-motivated conversion factors that link [C II] luminosity,  $L_{[\text{C II}]}$ , to H<sub>2</sub> mass ( $\alpha_{[\text{C II}]}$ ) and H I mass ( $\beta_{[\text{C II}]}$ ), as well as their scalings with stellar mass and SFR.

Our main findings can be summarized as follow:

1. COLDSIM results reproduce the [C II] luminosity function trends observed by ALMA. Our galaxies extend the [C II] luminosity function to  $L_{[\text{C II}]}$  lower than those accessible to observations at  $z = 6$ , providing first predictions in a range where data are still limited.
2. We find a linear relation between  $\log_{10}(L_{[\text{C II}]})$  and  $\log_{10}(M_{\text{H}_2})$  at all redshifts. Our results at  $z = 6$  are in agreement with observational estimates from galaxies in the range  $z = 0 - 7$ . In particular, the model by Madden et al. (2020), derived from local dwarf galaxies, broadly aligns with our estimates. It should nevertheless be noted that the range of  $M_{\text{H}_2}$  and  $L_{[\text{C II}]}$  analysed and/or observed is not always the same, and thus the comparison must refer to an extrapolation of the results.
3. We study also the relation between  $\log_{10}(L_{[\text{C II}]})$  and  $\log_{10}(M_{\text{HI}})$ . We find that for a fixed  $L_{[\text{C II}]}$  the mass of H I is typically  $\sim 2$  dex higher than that of H<sub>2</sub>.
4. The amplitude and the scatter of the mentioned relations evolve with redshift. We provide redshift-dependent fitting formulae that link  $L_{[\text{C II}]}$  to  $M_{\text{H}_2}$  and  $M_{\text{HI}}$ , and that can be used to estimate the mass of molecular and atomic gas of a galaxy from its (detected) [C II] luminosity.



5. We investigate the dependence of the  $\alpha_{[\text{C II}]}$  and  $\beta_{[\text{C II}]}$  conversion factors on the stellar metallicity,  $Z_{\star}$ , finding a good agreement with observational estimates at lower redshift. For  $Z_{\star} < 10^{-1} Z_{\odot}$ , the lack of carbon causes an increase of about 2 dex in the values of  $\alpha_{[\text{C II}]}$  and  $\beta_{[\text{C II}]}$  and this might help explain the common [C II] deficit in galaxies around  $z \simeq 7$  (consistently with observational findings by Glazer et al. 2024).
6. We explore the scatter in the relationship between  $\alpha_{[\text{C II}]}$  and  $Z_{\star}$ , finding that for metallicities  $Z_{\star} > 10^{-2} Z_{\odot}$ , the large scatter depends on the galaxy's SFR. Highly star-forming galaxies ionise carbon at higher ionisation states, making them less luminous in  $L_{[\text{C II}]}$  than galaxies with similar metallicity, but lower SFR.
7. We look at the contribution of each gas phase, ionised, neutral atomic and molecular, to the total emission in  $L_{[\text{C II}]}$ , and study the correlation with SFR and  $M_{\star}$ . We find that, for SFR  $> 10^{-2.5} M_{\odot} \text{ yr}^{-1}$  and  $M_{\star} > 10^5 M_{\odot}$ , the phase that dominates  $L_{[\text{C II}]}$  is the atomic one, with fractional contributions ranging from 70 to 90%.
8. The contribution from molecular gas varies, with values up to  $\sim 30\%$  for galaxies with SFR  $\gtrsim 10^{-1} M_{\odot} \text{ yr}^{-1}$  and  $M_{\star} \gtrsim 10^8 M_{\odot}$ . We notice that, even though  $L_{[\text{C II}]}$  traces largely H I gas, it is still extremely useful to estimate the mass of the sub-dominant molecular phase, due to the relatively small fluctuations of H<sub>2</sub> contributions across the considered mass range.
9. In the entire simulated volume, the vast majority of  $L_{[\text{C II}]}$  is predicted to get originated in warm dense and star-forming regions irrespectively of the redshift, in line with the latest observational results by Ikeda et al. (2024).

The work presented here offers new theoretical insights to study the processes responsible for the origin of [C II] 158  $\mu\text{m}$  fine-structure line emission during the epoch of reionization and supports recent and upcoming observations of star-forming gas in primordial times. However, to better link theory and observations future investigations are still required. They will be crucial to reach a full understanding of carbon chemical signatures in the first Gyr and interpret correctly the origin of the first galaxies at such primeval epochs.

*Acknowledgements.* We are thankful to Aniket Bhagwat for fruitful discussions on emission processes in high- $z$  galaxies. We are grateful to Rodrigo Herrera-Camus for providing a preview of the results on [C II] luminosity in the CRISTAL galaxies. BC thanks Victoria Bollo for the help in the CASA calculations and the interesting discussion about molecular gas emission and absorption features through cosmic time. UM acknowledges financial support from the theory grant no. 1.05.23.06.13 "FIRST – First Galaxies in the Cosmic Dawn and the Epoch of Reionization with High Resolution Numerical Simulations" and the travel grant no. 1.05.23.04.01 awarded by the Italian National Institute for Astrophysics. UM was supported in part by grant NSF PHY-2309135 to the Kavli Institute for Theoretical Physics (KITP), Santa Barbara (USA). This research was supported by the International Space Science Institute (ISSI) in Bern (Switzerland), through ISSI International Team project no. 564 (The Cosmic Baryon Cycle from Space). The numerical calculations done throughout this work have been performed on the machines of the Max Planck Computing and Data Facility of the Max Planck Society, Germany. We acknowledge the NASA Astrophysics Data System for making available their bibliographic research tool

## References

Abel, T., Anninos, P., Zhang, Y., & Norman, M. L. 1997, *New A*, 2, 181  
 Accurso, G., Saintonge, A., Catinella, B., et al. 2017, *MNRAS*, 470, 4750  
 Andreani, P., Miyamoto, Y., Kaneko, H., et al. 2020, *A&A*, 643, L11  
 Aravena, M., Decarli, R., Walter, F., et al. 2016, *ApJ*, 833, 71  
 Aravena, M., Heintz, K., Dessauges-Zavadsky, M., et al. 2024, *A&A*, 682, A24  
 Bakes, E. L. O. & Tielens, A. G. G. M. 1994, *ApJ*, 427, 822

B ethermin, M., Fudamoto, Y., Ginolfi, M., et al. 2020, *A&A*, 643, A2  
 Bisbas, T. G., Walch, S., Naab, T., et al. 2022, *ApJ*, 934, 115  
 Blitz, L. & Rosolowsky, E. 2006, *ApJ*, 650, 933  
 Bolatto, A. D., Wolfire, M., & Leroy, A. K. 2013, *ARA&A*, 51, 207  
 Boogaard, L. A., Decarli, R., Walter, F., et al. 2023, *ApJ*, 945, 111  
 Bouwens, R. J., Smit, R., Schouws, S., et al. 2022, *ApJ*, 931, 160  
 Capak, P. L., Carilli, C., Jones, G., et al. 2015, *Nature*, 522, 455  
 Cappellaro, E., Botticella, M. T., Pignata, G., et al. 2015, *A&A*, 584, A62  
 Carilli, C. L. & Walter, F. 2013, *ARA&A*, 51, 105  
 Casavecchia, B., Maio, U., P eroux, C., & Ciardi, B. 2024, arXiv e-prints, arXiv:2406.01277  
 Chabrier, G. 2003, *PASP*, 115, 763  
 CONCERTO Collaboration, Ade, P., Aravena, M., et al. 2020, *A&A*, 642, A60  
 Contursi, A., Baker, A. J., Berta, S., et al. 2017, *A&A*, 606, A86  
 Cormier, D., Abel, N. P., Hony, S., et al. 2019, *A&A*, 626, A23  
 Cormier, D., Madden, S. C., Lebouteiller, V., et al. 2015, *A&A*, 578, A53  
 Croxall, K. V., Smith, J. D., Pellegrini, E., et al. 2017, *ApJ*, 845, 96  
 Curtis-Lake, E., Carniani, S., Cameron, A., et al. 2023, *Nature Astronomy*, 7, 622  
 Daddi, E., Bournaud, F., Walter, F., et al. 2010, *ApJ*, 713, 686  
 Dav e, R., Crain, R. A., Stevens, A. R. H., et al. 2020, *MNRAS*, 497, 146  
 De Breuck, C., Wei , A., B ethermin, M., et al. 2019, *A&A*, 631, A167  
 De Looze, I., Cormier, D., Lebouteiller, V., et al. 2014, *A&A*, 568, A62  
 Decarli, R., Aravena, M., Boogaard, L., et al. 2020, *ApJ*, 902, 110  
 Decarli, R., Walter, F., G onzalez-L opez, J., et al. 2019, *ApJ*, 882, 138  
 Dessauges-Zavadsky, M., Ginolfi, M., Pozzi, F., et al. 2020, *A&A*, 643, A5  
 Di Cesare, C., Ginolfi, M., Graziani, L., et al. 2024, arXiv e-prints, arXiv:2401.03020  
 Diaz-Santos, T., Armus, L., Charmandaris, V., et al. 2017, *ApJ*, 846, 32  
 Diaz-Santos, T., Armus, L., Charmandaris, V., et al. 2013, *ApJ*, 774, 68  
 Dobbs, C. L. & Pringle, J. E. 2013, *MNRAS*, 432, 653  
 Draine, B. T. & Bertoldi, F. 1996, *ApJ*, 468, 269  
 Draine, B. T. & Sutn, B. 1987, *ApJ*, 320, 803  
 Dunne, L., Maddox, S. J., Papadopoulos, P. P., Ivison, R. J., & Gomez, H. L. 2022, *MNRAS*, 517, 962  
 Ebagezio, S., Seifried, D., Walch, S., et al. 2023, *MNRAS*, 525, 5631  
 Ferkinhoff, C., Brisbin, D., Parshley, S., et al. 2014, *ApJ*, 780, 142  
 Feruglio, C., Maio, U., Tripodi, R., et al. 2023, *ApJ*, 954, L10  
 Fukui, Y. & Kawamura, A. 2010, *ARA&A*, 48, 547  
 Galli, D. & Palla, F. 1998, *A&A*, 335, 403  
 Garcia, K., Narayanan, D., Popping, G., et al. 2023, arXiv e-prints, arXiv:2311.01508  
 Gelli, V., Mason, C., & Hayward, C. C. 2024, arXiv e-prints, arXiv:2405.13108  
 Genzel, R., Tacconi, L. J., Lutz, D., et al. 2015, *ApJ*, 800, 20  
 Gkogkou, A., B ethermin, M., Lagache, G., et al. 2023, *A&A*, 670, A16  
 Glazer, K., Brad c, M., Sanders, R. L., et al. 2024, *MNRAS*, 531, 945  
 Glover, S. C. O. & Clark, P. C. 2012, *MNRAS*, 421, 9  
 Gnedin, N. Y. & Draine, B. T. 2014, *ApJ*, 795, 37  
 Greggio, L. 2005, *A&A*, 441, 1055  
 Gullberg, B., De Breuck, C., Vieira, J. D., et al. 2015, *MNRAS*, 449, 2883  
 Gurman, A., Hu, C.-Y., Sternberg, A., & van Dishoeck, E. F. 2024, *ApJ*, 965, 179  
 Haardt, F. & Madau, P. 1996, *ApJ*, 461, 20  
 Habing, H. J. 1968, *Bull. Astron. Inst. Netherlands*, 19, 421  
 Hamaonowicz, A., Zwaan, M. A., P eroux, C., et al. 2023, *MNRAS*, 519, 34  
 Hassan, S. & Gronke, M. 2021, *ApJ*, 908, 219  
 Heintz, K. E., Watson, D., Oesch, P. A., Narayanan, D., & Madden, S. C. 2021, *ApJ*, 922, 147  
 Hemmati, S., Yan, L., Diaz-Santos, T., et al. 2017, *ApJ*, 834, 36  
 Hollenbach, D. & McKee, C. F. 1979, *ApJS*, 41, 555  
 Hu, C.-Y., Sternberg, A., & van Dishoeck, E. F. 2021, *ApJ*, 920, 44  
 Hu, C.-Y., Sternberg, A., & van Dishoeck, E. F. 2023, *ApJ*, 952, 140  
 Hughes, T. M., Ibar, E., Villanueva, V., et al. 2017, *A&A*, 602, A49  
 Huynh, M. T., Kimball, A. E., Norris, R. P., et al. 2014, *MNRAS*, 443, L54  
 Ikeda, R., Tadaki, K.-i., Mitsuhashi, I., et al. 2024, arXiv e-prints, arXiv:2408.03374  
 Kaasinen, M., Venemans, B., Harrington, K. C., et al. 2024, *A&A*, 684, A33  
 Katz, H., Galligan, T. P., Kimm, T., et al. 2019, *MNRAS*, 487, 5902  
 Keating, L. C., Richings, A. J., Murray, N., et al. 2020, *MNRAS*, 499, 837  
 Kennicutt, Robert C., J. 1998, *ApJ*, 498, 541  
 Klaassen, P. D., Mroczkowski, T. K., Ciccone, C., et al. 2020, in *Society of Photo-Optical Instrumentation Engineers (SPIE) Conference Series*, Vol. 11445, Ground-based and Airborne Telescopes VIII, ed. H. K. Marshall, J. Spyromilio, & T. Usuda, 114452F  
 Klitsch, A., P eroux, C., Zwaan, M. A., et al. 2019, *MNRAS*, 490, 1220  
 Kravtsov, A. & Belokurov, V. 2024, arXiv e-prints, arXiv:2405.04578  
 Krumholz, M. R. 2013, *MNRAS*, 436, 2747  
 Krumholz, M. R. 2014, *Phys. Rep.*, 539, 49  
 Krumholz, M. R. & Gnedin, N. Y. 2011, *ApJ*, 729, 36  
 Lagache, G., Cousin, M., & Chatzikos, M. 2018, *A&A*, 609, A130  
 Lagos, C. d. P., Crain, R. A., Schaye, J., et al. 2015, *MNRAS*, 452, 3815  
 Le F evre, O., B ethermin, M., Faisst, A., et al. 2020, *A&A*, 643, A1

- Lepp, S. & Shull, J. M. 1983, *ApJ*, 270, 578
- Leroy, A. K., Walter, F., Brinks, E., et al. 2008, *AJ*, 136, 2782
- Liang, L., Feldmann, R., Murray, N., et al. 2024, *MNRAS*, 528, 499
- Lupi, A. & Bovino, S. 2020, *MNRAS*, 492, 2818
- Madden, S. C., Cormier, D., Honý, S., et al. 2020, *A&A*, 643, A141
- Magdis, G. E., Rigopoulou, D., Hopwood, R., et al. 2014, *ApJ*, 796, 63
- Maio, U., Borgani, S., Ciardi, B., & Petkova, M. 2019, *PASA*, 36, e020
- Maio, U., Ciardi, B., Dolag, K., Tornatore, L., & Khochfar, S. 2010, *MNRAS*, 407, 1003
- Maio, U., Ciardi, B., Yoshida, N., Dolag, K., & Tornatore, L. 2009, *A&A*, 503, 25
- Maio, U., Dolag, K., Ciardi, B., & Tornatore, L. 2007, *MNRAS*, 379, 963
- Maio, U., Dolag, K., Meneghetti, M., et al. 2006, *MNRAS*, 373, 869
- Maio, U., Khochfar, S., Johnson, J. L., & Ciardi, B. 2011a, *MNRAS*, 414, 1145
- Maio, U., Koopmans, L. V. E., & Ciardi, B. 2011b, *MNRAS*, 412, L40
- Maio, U., Péroux, C., & Ciardi, B. 2022, *A&A*, 657, A47
- Maio, U., Petkova, M., De Lucia, G., & Borgani, S. 2016, *MNRAS*, 460, 3733
- Maio, U. & Viel, M. 2015, *MNRAS*, 446, 2760
- Maio, U. & Viel, M. 2023, *A&A*, 672, A71
- Maoz, D. & Graur, O. 2017, *ApJ*, 848, 25
- McElroy, D., Walsh, C., Markwick, A. J., et al. 2013, *A&A*, 550, A36
- McMullin, J. P., Waters, B., Schiebel, D., Young, W., & Golap, K. 2007, in *Astronomical Society of the Pacific Conference Series*, Vol. 376, *Astronomical Data Analysis Software and Systems XVI*, ed. R. A. Shaw, F. Hill, & D. J. Bell, 127
- Mitsuhashi, I., Tadaki, K.-i., Ikeda, R., et al. 2023, *arXiv e-prints*, arXiv:2311.17671
- Muñoz-Elgueta, N., Arrigoni Battaia, F., Kauffmann, G., et al. 2024, *arXiv e-prints*, arXiv:2407.17359
- Nagamine, K., Springel, V., & Hernquist, L. 2004, *MNRAS*, 348, 421
- Olsen, K., Greve, T. R., Narayanan, D., et al. 2017, *ApJ*, 846, 105
- Olsen, K., Greve, T. R., Narayanan, D., et al. 2018, *ApJ*, 857, 148
- Pallottini, A., Ferrara, A., Bovino, S., et al. 2017, *MNRAS*, 471, 4128
- Pallottini, A., Ferrara, A., Decataldo, D., et al. 2019, *MNRAS*, 487, 1689
- Patrick, S. J., Whalen, D. J., Latif, M. A., & Elford, J. S. 2023, *MNRAS*, 522, 3795
- Péroux, C. & Howk, J. C. 2020, *ARA&A*, 58, 363
- Péroux, C., Zwaan, M. A., Klitsch, A., et al. 2019, *MNRAS*, 485, 1595
- Pineda, J. L., Langer, W. D., Velusamy, T., & Goldsmith, P. F. 2013, *A&A*, 554, A103
- Popping, G., Narayanan, D., Somerville, R. S., Faisst, A. L., & Krumholz, M. R. 2019, *MNRAS*, 482, 4906
- Popping, G. & Péroux, C. 2022, *MNRAS*, 513, 1531
- Ramos Padilla, A. F., Wang, L., Ploekinger, S., van der Tak, F. F. S., & Trager, S. C. 2021, *A&A*, 645, A133
- Ramos Padilla, A. F., Wang, L., van der Tak, F. F. S., & Trager, S. C. 2023, *A&A*, 679, A131
- Rémy-Ruyer, A., Madden, S. C., Galliano, F., et al. 2014, *A&A*, 563, A31
- Riechers, D. A., Pavesi, R., Sharon, C. E., et al. 2019, *ApJ*, 872, 7
- Righi, M., Hernández-Monteagudo, C., & Sunyaev, R. A. 2008, *A&A*, 489, 489
- Roussel, H., Helou, G., Hollenbach, D. J., et al. 2007, *ApJ*, 669, 959
- Roy, A. & Lapi, A. 2024, *arXiv e-prints*, arXiv:2407.19007
- Saintonge, A., Catinella, B., Tacconi, L. J., et al. 2017, *ApJS*, 233, 22
- Saintonge, A., Kauffmann, G., Kramer, C., et al. 2011, *MNRAS*, 415, 32
- Salpeter, E. E. 1955, *ApJ*, 121, 161
- Saslaw, W. C. & Zipoy, D. 1967, *Nature*, 216, 976
- Schaerer, D., Boone, F., Jones, T., et al. 2015, *A&A*, 576, L2
- Schaerer, D., Ginolfi, M., Béthermin, M., et al. 2020, *A&A*, 643, A3
- Schimek, A., Decataldo, D., Shen, S., et al. 2024, *A&A*, 682, A98
- Sommovigo, L., Ferrara, A., Carniani, S., et al. 2021, *MNRAS*, 503, 4878
- Springel, V. 2005, *MNRAS*, 364, 1105
- Springel, V. & Hernquist, L. 2003, *MNRAS*, 339, 289
- Stacey, G. J., Geis, N., Genzel, R., et al. 1991, *ApJ*, 373, 423
- Szakacs, R., Péroux, C., Zwaan, M., et al. 2021, *MNRAS*, 505, 4746
- Szakacs, R., Péroux, C., Zwaan, M. A., et al. 2022, *MNRAS*, 512, 4736
- Tacconi, L. J., Genzel, R., Saintonge, A., et al. 2018, *ApJ*, 853, 179
- Tacconi, L. J., Genzel, R., & Sternberg, A. 2020, *ARA&A*, 58, 157
- Tacconi, L. J., Neri, R., Genzel, R., et al. 2013, *ApJ*, 768, 74
- Telford, O. G., McQuinn, K. B. W., Chisholm, J., & Berg, D. A. 2023, *ApJ*, 943, 65
- Tinsley, B. M. 1980, *Fund. Cosmic Phys.*, 5, 287
- Togi, A. & Smith, J. D. T. 2016, *ApJ*, 830, 18
- Tornatore, L., Borgani, S., Dolag, K., & Matteucci, F. 2007, *MNRAS*, 382, 1050
- Vallini, L., Gallerani, S., Ferrara, A., Pallottini, A., & Yue, B. 2015, *ApJ*, 813, 36
- Vizgan, D., Greve, T. R., Olsen, K. P., et al. 2022a, *ApJ*, 929, 92
- Vizgan, D., Heintz, K. E., Greve, T. R., et al. 2022b, *ApJ*, 939, L1
- Walter, F., Neeleman, M., Decarli, R., et al. 2022, *ApJ*, 927, 21
- Williams, C. E., Lake, W., Naoz, S., et al. 2024, *ApJ*, 960, L16
- Witten, C., McClymont, W., Laporte, N., et al. 2024, *arXiv e-prints*, arXiv:2407.07937
- Woods, T. E., Patrick, S., Whalen, D. J., & Heger, A. 2024, *ApJ*, 960, 59
- Yamaguchi, Y., Kohno, K., Tamura, Y., et al. 2017, *ApJ*, 845, 108
- Yan, L., Sajina, A., Loiacono, F., et al. 2020, *ApJ*, 905, 147
- Yang, S., Popping, G., Somerville, R. S., et al. 2022, *ApJ*, 929, L1
- Yoshida, N., Sokasian, A., Hernquist, L., & Springel, V. 2003, *ApJ*, 591, L1
- Zanella, A., Daddi, E., Magdis, G., et al. 2018, *MNRAS*, 481, 1976